Published in final edited form as:

Nat Methods. 2021 September ; 18(9): 1103–1111. doi:10.1038/s41592-021-01239-8.

High-speed, cortex-wide volumetric recording of neuroactivity at cellular resolution using light beads microscopy

Jeffrey Demas[1,2], **Jason Manley**[1,2], **Frank Tejera**[1], **Kevin Barber**[1], **Hyewon Kim**[1], **Francisca Martínez Traub**[1], **Brandon Chen**[1], **Alipasha Vaziri**[1,2,✉]

[1]Laboratory of Neurotechnology and Biophysics, The Rockefeller University, New York, NY, USA.

[2]The Kavli Neural Systems Institute, The Rockefeller University, New York, NY, USA.

Abstract

Two-photon microscopy has enabled high-resolution imaging of neuroactivity at depth within scattering brain tissue. However, its various realizations have not overcome the tradeoffs between speed and spatiotemporal sampling that would be necessary to enable mesoscale volumetric recording of neuroactivity at cellular resolution and speed compatible with resolving calcium transients. Here, we introduce light beads microscopy (LBM), a scalable and spatiotemporally optimal acquisition approach limited only by fluorescence lifetime, where a set of axially separated and temporally distinct foci record the entire axial imaging range near-simultaneously, enabling volumetric recording at 1.41×10^8 voxels per second. Using LBM, we demonstrate mesoscopic and volumetric imaging at multiple scales in the mouse cortex, including cellular-resolution recordings within ~3 × 5 × 0.5 mm volumes containing >200,000 neurons at ~5 Hz and recordings of populations of ~1 million neurons within ~5.4 × 6 × 0.5 mm volumes at ~2 Hz, as well as higher speed (9.6 Hz) subcellular-resolution volumetric recordings. LBM provides an opportunity for discovering the neurocomputations underlying cortex-wide encoding and processing of information in the mammalian brain.

Two-photon microscopy (2pM)[1–3] with genetically encodable calcium indicators (GECIs)[4–6] has emerged as the standard technique for imaging neuronal activity at depth within

✉ vaziri@rockefeller.edu.

Author contributions

J. D. contributed to the project conceptualization, designed and built the imaging and data acquisition system, performed experiments, programmed experimental control and analysis software, analyzed data, and wrote the manuscript. J. M. performed data processing and modeling and contributed to writing the manuscript. F. T. contributed to microscope construction and characterization and aided in developing the experimental control design. H. K., F. M. T., and B. C. performed virus injections and cranial window surgeries. K. B. performed immunohistochemistry experiments. A. V. conceived and led the project, designed the imaging system, the data acquisition approach, and all in vivo mouse experiments, guided data analysis, and wrote the manuscript.

Competing interests

A. V. and J. D. described Light Beads Microscopy in patent application PCT/US2021/015957.

Additional information

Extended data is available for this paper at https://doi.org/10.1038/s41592-021-01239-8.

Supplementary information The online version contains supplementary material available at https://doi.org/10.1038/s41592-021-01239-8.

Correspondence and requests for materials should be addressed to A.V.

Peer review information *Nature Methods* thanks Rosa Cossart and the other, anonymous, reviewer(s) for their contribution to the peer review of this work.

scattering brain tissue. However, anatomical and functional observations suggest that complex brain functions emerge from highly parallel computation[7,8] in which sensory information[9,10] and behavioral parameters[11,12] are mapped onto brain-wide neuronal populations[13–16] at scales beyond the fields of view (FOVs) of conventional microscopes (<0.5 mm). Maximizing volumetric FOVs (v-FOVs) toward brain-wide imaging requires both mesoscopic optical access and optimal spatiotemporal sampling, such that information is obtained as fast as possible, each voxel provides information at sufficient signal-to-noise ratio (SNR), and the microscope records only the minimum amount of information necessary to resolve features of interest (for example, cell bodies) in order to devote remaining resources to imaging the largest possible volumes at time scales compatible with calcium imaging.

Many 2pM platforms have demonstrated mesoscopic optical performance[17–23], however in these systems, spatiotemporal sampling remains suboptimal: the high-repetition-rate lasers typically employed lead to oversampling in the lateral plane and the need for multiple pulses per pixel to improve SNR at low pulse energies. Accordingly, performance is limited to, at most, multiplane rather than volumetric performance, slow frame rates, and low SNR, particularly when imaging at depth. As we have argued previously[24,25], single-pulse-per-voxel acquisition maximizes SNR per unit power delivered to the brain, and additionally, sampling at the minimum lateral density dictated by the application frees up temporal resources toward scaling the v-FOV.

Another approach for scaling the v-FOV is using parallel excitation to increase the information rate. Some systems employ laterally[26] or axially[27–29] extended point-spread functions (PSFs) to form projections of the volume such that only two-dimensional scanning is required, whereas others excite multiple sample locations simultaneously, using spatially resolved detection to reconstitute images[30,31]. However, these approaches suffer from scattering-mediated crosstalk at depth, and work best for sparsely labeled samples, reducing applicability to imaging large networks.

Temporal multiplexing[19,23,25,32–34] can be used to increase information throughput by scanning n copies of a single laser pulse, which are delayed in time and directed toward separate regions of the sample. For beam-to-beam delays exceeding the fluorescence lifetime (~6–7 ns for GCaMP[33]), fluorescence at the detector can be reassigned to reconstitute the FOV scanned by each beam, resulting in an n-fold increase in data rate. However, multiplexed systems employing typical Ti:Sapphire lasers (~80 MHz repetition rate) are limited to, at most, a roughly twofold increase in data rate[19,23,32–34] and suffer from the oversampling inefficiencies mentioned above. Lowering laser repetition rates to the few-MHz regime can simultaneously increase the maximum possible degree of multiplexing n and improve sampling efficiency[25]. However, many multiplexing platforms require chains of beam splitters and dedicated optical paths for delaying and steering each beam, resulting in the unfavorable scaling of system complexity with increasing n[10,19,23,25,33,34] and leaving the majority of the interpulse timing interval unexploited[25]. Recently, multipass temporal multiplexing schemes have been demonstrated, in which beams undergo multiple round trips through a single set of components that tag the light with a specific delay and focal position in the sample corresponding to each pass through the system[35,36]. While using a

multipass design, it is in principle possible to achieve higher degrees of multiplicity at a reduced optical complexity, but current realizations either exhibit a fundamentally limited potential for an increase in multiplicity[36] or are inconsistent with one-pulse-per-voxel excitation[10,35,37].

Here we demonstrate LBM: a high-speed optical acquisition technique for mesoscopic and volumetric 2pM. In LBM, the microscope scans a set of axially separated and temporally distinct foci ('beads') as opposed to a single focus (Fig. 1a). The beads record information throughout the entire depth range of the sample (~500 μm) within the deadtime between subsequent pulses of the laser (~200 ns), thus LBM can probe entire volumes within the time it takes to scan a single plane. Furthermore, by using efficient spatial sampling, LBM allows for expansion of v-FOVs to mesoscopic scales while retaining GCaMP-compatible volume rates. Our light beads are formed by a cavity-based multiplexing approach called the many-fold axial multiplexing module (MAxiMuM) that allows for scaling of the multiplicity limited by only the fluorescence lifetime of GCaMP and the interpulse interval of the laser. Crucially, MAxiMuM also allows for flexible control of the relative power and position of each beam. Using MAxiMuM, we demonstrate 30-fold axial multiplexing and a voxel acquisition rate of 141 MHz with ~16-μm plane-to-plane axial separation, conditions that are optimized for, and compatible with, sampling densely labeled tissue volumes at fluorescence-lifetime-limited rates, with one-pulse-per-voxel SNR-maximized excitation while utilizing the entire interpulse time interval.

We have realized the design of our LBM on a mesoscopy platform that allows access to a ~6 × 6 mm^2 FOV at subcellular resolution (0.6 numerical aperture)[18], demonstrating volumetric and single-cell-resolution recording from volumes of ~3 × 5 × 0.5 mm, encompassing portions of the visual (VISp), somatosensory (SSp), posterior parietal (PTLp), and retrosplenial (RSP) areas of GCaMP6s-labeled[6,38] mouse neocortex at a ~5-Hz volume rate. Additionally, we highlight the versatility of LBM on this platform by recording in a variety of configurations, ranging from moderately sized FOVs (600 × 600 × 500 μm) with voxel resolution capable of resolving subcellular features to FOVs (5.4 × 6 × 0.5 mm) encompassing both hemispheres of the mouse cortex and capturing the dynamics of populations exceeding 1,000,000 neurons. We find that correlated activity of neurons in these experiments have characteristic lengths $\gg$ 1 mm. Stimulus- and behavior-tuned populations captured by LBM exhibit richly varied responses at the single-trial level—including subpopulations with correlated trial-to-trial variations in their responses—underlining the need for such volumetric and mesoscopic calcium-imaging techniques to understand real-time neurocomputations performed by intercortical circuitry.

Results

Light bead generation with MAxiMuM.

MAxiMuM is a stand-alone unit that generates columns of light beads that can be interfaced with any given microscope. Laser light is focused above a partially reflective mirror (PRM) at the entrance of the cavity and is subsequently re-imaged by a series of concave mirrors (Fig. 1b and Extended Data Figs. 1 and 2). An intentional offset Δz between the nominal focus of the re-imaging mirrors and the input of the cavity results in an axial shift in the

beam's focus as the beam returns to the entrance. Before reaching the cavity entrance, the beam encounters the PRM, which reflects the majority of light back into the cavity for another round trip, with a small lateral offset relative to the first beam. The remaining fraction of the light couples out of the cavity and is sent toward the microscope. Owing to the axial offset, each beam exiting the cavity focuses to a shallower depth in the sample, with a relative decrease in optical power such that the power in the ith beam is given by $P_i \propto T(1-T)^i$, where T is the transmission of the PRM.

Maintaining constant SNR over the imaged depth range requires an exponential increase in laser power for deeper foci due to loss of ballistic photons in scattering tissue. To achieve this, we adjusted the transmission of the cavity, T, such that the relative power increase between subsequent beams matches the increase required to offset additional tissue scattering due to the axial separation between adjacent planes, δz, resulting in constant SNR for all multiplexed beams. This condition is given by:

$$T = 1 - \exp\left(-\frac{\delta z}{l_s}\right) \quad (1)$$

where l_s is the scattering mean free path of brain tissue (~200 μm for at 960 nm[39]), and the relationship between the axial separation of beams exiting the cavity (Δz) and those in the sample (δz) is given by $\Delta z = M^2 \times \delta z$, with M being the magnification of the microscope. Equation 1 provides a design rule for achieving a given axial sampling density with LBM (Supplementary Note 1). This design flexibility represents a distinguishing feature of LBM and a key difference compared with reverberation microscopy[36], where, owing to the fixed transmission of 50%, maintaining SNR requires an axial separation of ~100 μm, limiting multiplicity to a handful of beams within the penetration depth of 2pM.

We integrated our LBM approach into an existing mesoscope (Extended Data Fig. 3) and characterized each light bead in sample space (Extended Data Fig. 4 and Supplementary Note 2) to ensure desired temporal and spatial characteristics. Through these calibrations, we confirmed fluorescence-lifetime-limited bead-to-bead delays (6.7 ns), minimal crosstalk between channels, linear sampling over the total axial range of ~500 μm, and lateral and axial diameters of ~1 μm and ~13 μm, respectively, for each light bead, which is sufficient for cellular-resolution imaging of densely labeled samples.

Optimization of spatiotemporal sampling efficiency.

In order to maximize spatiotemporal sampling efficiency and record from the largest possible FOV, only the minimum amount of information necessary to faithfully extract features of interest—in our case, neuronal cell bodies—should be recorded. To explore this limit systematically, we conducted in vivo experiments in the neocortex of GCaMP6f-expressing mice. We recorded several high-resolution single-plane data sets and fed them into our analysis pipeline (Extended Data Fig. 5 and Supplementary Note 3), comparing the extracted footprints and time series to manually segmented ground truths for each data set. Using F-score (defined as the harmonic mean of the true- and false-positive rates) as a metric for extraction fidelity, we evaluated how performance deteriorates with increasing sampling sparsity by removing pixels from the lateral image stacks. Consistent with our

previous results[24,25], we found that the *F*-score only detrimentally declines for lateral spatial sampling >5 μm (Extended Data Fig. 6a). Thus, to maximize the imaging volume while maintaining extraction fidelity, we found an optimum sampling of ~5 μm in the lateral plane.

Multiregional and multisensory imaging of activity from >200,000 neurons in mouse cortex.

We validated LBM in vivo by recording from the neocortex of awake and behaving mice that transgenically expressed GCaMP6s in glutamatergic neurons[6,38]. Using our optimized spatial sampling strategy, we could maintain a volume rate of ~5 Hz within a volume of ~3 × 5 × 0.5 mm, allowing us to resolve GCaMP transients. We chose placement of our v-FOV to encompass as many distinct regions as possible within a single cortical hemisphere including SSp and PTLp, as well as RSP and VISp (Fig. 2a), at depths corresponding to layers I through IV (Fig. 2b). We employed a dual-sensory stimulus paradigm in these recordings, consisting of perturbation of whiskers contralateral to the imaged hemisphere and presentation of high-contrast drifting gratings. We placed animals on a treadmill equipped with motion tracking and video-based behavioral tracking that allowed us to capture any movements of the hind or forelimbs that lacked correlation with the above controlled stimuli (Supplementary Video 1). We refer to any such movement as a spontaneous behavior in subsequent analyses.

In this modality, we could record from ~200,000 neurons distributed across a ~500 μm axial range within the cortical regions mentioned above (volume rendering in Fig. 2a and Supplementary Video 2). As expected (Extended Data Fig. 6), and consistent with the spatiotemporal characteristics of our light beads (Extended Data Fig. 4), we could indeed resolve individual neurons (Fig. 2c,d and Supplementary Videos 3 and 4), allowing for extraction of their time series (Extended Data Fig. 7 and Supplementary Video 5). The time scale of the observed calcium transients is consistent with the response time of GCaMP6s (Extended Data Fig. 8) and shows correlations with both visual and whisker stimuli.

We computed the distribution of correlations between the time series of each neuron and the stimuli presentation, that is the whisker trials and the visual trials, as well as correlation with spontaneous animal behaviors (Extended Data Fig. 9a–c). We found subpopulations of neurons spanning many regions of the cortex (Fig. 3a–e) that were highly tuned to each stimulus ($R > 3\sigma$), numbering 34,468 whisker-tuned neurons, 24,299 visually tuned neurons, and 64,810 neurons tuned to uninstructed animal behaviors. We performed hierarchical clustering on the correlation matrix of the population of all 123,577 stimulus-tuned neurons (Extended Data Fig. 9d) and found 4 distinct clusters, each exhibiting a different axial distribution across depth (Extended Data Fig. 9e–i). We subsequently mapped these clusters, and the neurons within them, back to their anatomical locations in the brain. For each population of neurons tuned to a stimulus modality (whisker or visual stimulation) or to uninstructed spontaneous behavior, we considered the relative size and location of the subpopulations corresponding to each cluster (Fig. 3b–d). For comparison, we also considered the lateral distribution of 13,259 neurons uncorrelated with any stimulus condition or the uninstructed spontaneous behavior ($|R| < \sigma$, Fig. 3e). For the majority of the stimulus conditions, we observed a distribution of correspondingly tuned neurons across

multiple regions of the cortex (Fig. 3a). For each condition, as well as for the uncorrelated population, we could faithfully extract the transients of single cells (Fig. 3f–i).

Cluster 1 (blue) was located primarily in the barrel field (SSp BFD) and PTLp (Fig. 3a), and was thus highly represented in the whisker-tuned population (Fig. 3b). This cluster was also highly represented in the population correlated with spontaneous behaviors (Fig. 3d), inferring mixed responses of the neurons in this cluster to both stimuli. Cluster 2 (green) was only represented in behavior-tuned neurons (Fig. 3d) and was primarily located in specialized regions of the SSp related to sensation in the lower limbs, upper limbs, and torso of the animal (SSp-LL, SSp-UL, and SSp-TR, respectively), as well as PTLp (Fig. 3a). Cluster 3 (yellow) was located in VISp and PTLp, and represented neurons correlated with all stimulus conditions. The final cluster 4 (red) was distributed across multiple regions, including SSp, VISp, PTLp, and a dense population within RSP, which is thought to be associated with spatial memory encoding[40]. This subset located within RSP was primarily tuned to spontaneous behaviors (Fig. 3d). The spatial clustering analysis suggests that, although some of these functional clusters overlap with distinct anatomical regions of the brain, neurons in these regions can also jointly represent multiple stimulus conditions or may have stimulus-evoked activity that is modulated by the presence of additional stimuli.

To further probe mixed representation, we analyzed the trial-averaged activity of stimulus-tuned neurons. First, we considered differences in activity for whisker-tuned neurons in trials in which only whisker stimuli were present and compared them with those in which we presented both whisker and visual stimuli together (Fig. 3j–l). The presence of a coincident visual trial resulted in populations of neurons with both positively (Fig. 3j) and negatively (Fig. 3k) modulated activity relative to trials with only whisker stimulation. We found similar numbers of positively (3,703) and negatively modulated (4,166) neurons (significance defined by all neurons for which $P < 0.05$ determined by a two independent sample *t*-test); however, there was a clear distinction between the anatomical location of the two populations, with positively modulated neurons located primarily in SSp BFD and negatively modulated neurons located in VISp. Figure 3m shows a map of visually tuned neurons with activity that was significantly modulated (all neurons with $P < 0.05$, two independent sample *t*-test) by coincident presentation of whisker stimuli. Visually tuned neurons were primarily negatively modulated by the presence of whisker stimuli and located within VISp. Figure 3n,o shows the population of whisker-tuned and visually tuned neurons that were significantly modulated (all neurons with $P < 0.05$, two independent sample *t*-test) by coincident uninstructed spontaneous behaviors of the animal. In both cases, the majority of whisker-tuned and visually tuned neurons are positively modulated by spontaneous behaviors.

Additionally, at the single-trial level, stimulus- and behavior-tuned populations showed both neuron-to-neuron and trial-to-trial variation. Figure 3p shows example traces from eight neurons tuned to whisker stimuli with coincident presentation of visual stimuli. In some instances, neurons anatomically separated by >1 mm exhibit variations in activity across trials that are correlated (neurons 1–4); in other instances, the variations in trial-to-trial activity do not covary with the above group nor with one another (neurons 5–8). At the population level, we found trial-to-trial correlations among whisker-tuned

neurons (Extended Data Fig. 9j) and visually tuned neurons (Extended Data Fig. 9k) to be positively skewed ($r = 0.16 \pm 0.24$ and $r = 0.26 \pm 0.29$, respectively) and consistent with previously measured values[41], with neuron-to-neuron separations spanning millimeter scales (Extended Data Fig. 9l) and multiple layers of the cortex (Extended Data Fig. 9m). Such trial-to-trial covariations of neuronal responses, also referred to as noise correlations, have been suggested to represent distributed, higher-dimensional information encoding the underlying interaction of external stimuli and behavioral states with internal states[11,42]. Noise correlations occur on a trial-by-trial basis and any trial averaging will prevent their detection. Thus, while sequential single-plane and tiled-FOV recordings could potentially capture the same population of cells shown here, the trial-to-trial variability of their responses recorded by our method would be lost.

Additionally, single-trial neuronal responses showed variability in the sequence of neuronal firing times across the brain (Fig. 3q). We quantified this variability by calculating the lag between the occurrence of spontaneous animal behaviors and the onset of stimulus-evoked activity, finding a ~1.7-second delay between the timing of the earliest- and latest-firing neurons. Figure 3r shows a heatmap of the lag variation in behavior-tuned neurons, while Fig. 3s shows the lateral positions of this population color-coded by relative lag (Supplementary Video 6). The earliest-responding neurons are primarily located in the SSp-TR, SSp-LL, and SSp-UL regions, whereas neurons in regions farther from these sensory areas, including RSP, PTLp, SSp BFD, and VISp, respond later, in keeping with previous results[11]. Correlated neurons in these data can span mesoscale separations of 2–4 mm (Fig. 3t), exhibit correlated trial-to-trial variations spanning different regions of the brain, and have spatiotemporal coding structure evident at calcium-scale time resolution, underscoring the need for high-speed, large-FOV, volumetric recording capability.

Re-configurable multi-scale imaging with LBM.

LBM maintains the ability to navigate tradeoffs between lateral voxel sampling, FOV, and imaging speed to suit numerous applications. For example, Fig. 4a–c shows mean projection images and example neuronal traces from a volume of ~600 × 600 × 500 μm^3 in the PTLp of a jGCaMP7f[43]-expressing mouse (Supplementary Video 7) at ~10-Hz volume rate and 1-μm lateral voxel sampling, sufficient for resolving subcellular features such as the neuronal processes of active cells. Relaxing voxel sampling to an intermediate ~3-μm lateral sampling (Fig. 4d–g and Supplementary Videos 8 and 9) allows for increasing the v-FOV to ~2.0 × 2.0 × 0.5 mm, containing a population of ~70,000 neurons that can be recorded at 6.5 Hz.

Finally, by employing ~5-μm lateral voxel sampling, we could image a volume of ~5.4 × 6.0 × 0.5 mm encompassing both hemispheres of the mouse neocortex down to a depth of ~600 μm in tissue (Fig. 5 and Supplementary Videos 10 and 11). Experiments in this modality used up to ~450 mW of optical power; however, we confirmed through immunohistochemical labeling experiments that, owing to the large cranial windows and mesoscale v-FOVs employed in these experiments, the optical power used did not result in any heating-related damage to the brain (Extended Data Fig. 10 and Supplementary Note 5). Figure 5a,b shows a representative recording in this modality, capturing 1,065,289 neurons at 2.2-Hz volume rate. Even with the reduced acquisition rate in this modality, the *F*-score

is preserved (Extended Data Fig. 6a), and thus calcium transients can still be detected and extracted (Fig. 5c, Extended Data Fig. 7c,d, and Supplementary Video 12). The optical access, large degree of multiplexing, and efficient scanning approach employed by LBM opens the door to scaling 2pM from single-brain-region to cortex-wide recording, allowing for investigation of bihemispheric cognitive processing, as well as capturing the dynamics of populations of neurons more than two orders of magnitude larger than what can be captured by other techniques[10,23,25,29].

Discussion

Mesoscopic 2pM platforms are necessary for increasing the optical access of calcium imaging to multiregional recording from the mammalian brain. However, as we argue and demonstrate, a spatiotemporal-sampling approach that optimizes the tradeoffs between speed, volume size, and resolution is essential to maximize the number of neurons that can be recorded simultaneously from ever-increasing v-FOVs (Supplementary Note 1). Such optimal sample acquisition requires one-pulse-per-voxel sample excitation, fluorescence-life-time limited excitation rates using the entire pulse-to-pulse interval, and spatial sampling at the minimum density required to resolve cells or other features of interest. This in turn frees up resources that can be used to further increase volume size, speed, or resolution.

LBM represents the first realization of the optimal condition described above. MAxiMuM allows for scaling of the multiplicity beyond the previously shown few-beam regime, making full use of the pulse-to-pulse time interval of our laser to achieve the maximum possible voxel rate within the fluorescence lifetime limit of GCaMP. Thereby, compared with existing techniques, LBM allows for an effective increase by up to an order of magnitude in the total number of accessed voxels, and an increase of one to two orders of magnitude in recording volume, scaling the total number of recorded neurons by up to three orders of magnitude while maintaining calcium-imaging-compatible frame rates (Supplementary Table 1).

In our current implementation of LBM, our depth reach is limited by the detected fluorescence signal but not the background surface fluorescence induced by 2p excitation. We envision that, by using a laser with shorter pulses as well as high-bandwidth amplification between the detector and digitizer, SNR could be enhanced to enable deeper imaging. Additionally, LBM could be combined with three-photon microscopy in a hybrid configuration[25] and thus could access sub-cortical regions. Finally, LBM is also compatible with employing an enlarged, temporally focused PSF, which would further increase the sensitivity of our method and the number of neurons detected.

Enabled by the capabilities of LBM, we have observed evidence of mixed selectivity[44] in large populations of neurons distributed across many brain regions, as well as trial-to-trial variability of both stimulus- and behavior-tuned neurons. Additionally, we found evidence for covariance of activity among subsets of the stimulus-tuned neuronal population across the brain at the single-trial level, which have been suggested to represent encoding of information about internal states and uncontrolled aspects of stimuli and behavior[11,42]. These observations highlight the need for both high-speed and large-

scale neuronal-recording capability in order to identify and capture long-range functional cortical circuits and the variability of their response at the trial-to-trial level and single-neuron resolution. Furthermore, the volumetric nature of the LBM technique offers opportunities for investigation and validation of different models of cortical organization and computation based on multi-layer and multiregional processing of information[13]. Moreover, as suggested by our observations on the correlation distance for the simple sensory and behavioral paradigms used in this work (2–4 mm), and bolstered by other findings[9,16,42], mesoscopic-scale volumetric imaging of populations on the order of 1×10^5–1×10^6 neurons is necessary for revealing the full neuronal population code in individual cortical regions[9,16,42,45], as well as identifying the structure and dynamics[11,13,46–48] of inter-regional brain activity critical for learning[12,49], memory[14,50], and other cognitive functions. As such, the size of the neuronal population recording enabled by our technique opens up a range of opportunities to understand how the neurocomputations underlying multiregional encoding and processing of sensory and behavioral information emerge from the dynamic interaction of brain-wide networks of neurons at the single-neuron level in the mammalian brain.

online content

Any methods, additional references, Nature Research reporting summaries, source data, extended data, supplementary information, acknowledgements, peer review information; details of author contributions and competing interests; and statements of data and code availability are available at https://doi.org/10.1038/s41592-021-01239-8.

Methods

Laser source.

Our custom laser system comprised an ultrafast ytterbium-doped fiber master oscillator and chirped-pulse amplifier (Active Fiber Systems, 60 W average power, 4.7 MHz, 300 fs pulse duration, ~10 μJ pulse energy, λ = 1,030 nm), followed by an optical parametric chirped-pulse amplifier (OPCPA, White Dwarf dual, Class5 Photonics). The OPCPA operated at a wavelength of 960 nm with ~90 fs duration pulses up to ~0.8 μJ in energy at a repetition rate of 4.7 MHz. We employed an electro-optic modulator (Conoptics, 350–160-BK) to dynamically adjust laser power in the sample and blank the beam while the resonant scanner was reversing direction. We pre-compensated pulse-broadening using two pairs of chirped mirrors (Class5 Photonics) with −500 fs^2 per reflection, which imparted a total of −24,000 fs^2 of anomalous group delay dispersion to counteract the material dispersion of the multiplexing module, the mesoscope, and the other components in the system. The tradeoffs regarding the repetition rate of the laser and characteristics of the MAxiMuM cavity are discussed in detail in Supplementary Note 1.

Spatiotemporal multiplexing module.

To facilitate spatiotemporal multiplexing, we constructed a cavity comprising concave mirrors configured in an 8-f, non-inverting, re-imaging scheme (Extended Data Fig. 1a). The input beam was focused by L_1, just above the aperture of the partially reflective mirror (PRM), M_1, and in the front focal plane of M_2. Mirrors M_2−M_5 were concave mirrors (*f*

= 500 mm, 2″ diameter) with custom low-dispersion dielectric coatings (Layertec), which re-imaged the initial spot onto the turning mirror M_6. M_6 provided a slight vertical tilt to the beam such that it intersected the PRM M_1. M_1 was a low-dispersion ultrafast beam splitter (Thorlabs, UFBS9010) with a nominal transmission of ~10% at 45° incidence. By adjusting the position of M_6, we were able to change the angle of incidence at the PRM and tune the transmission to the desired value of ~8%. The majority of the light incident on M_1 underwent the next round trip through the cavity, and the rest of the light was transmitted. Each round trip through the cavity provided a temporal delay $\tau = 13.8$ ns, as well as an offset in the focal plane of the beam, dictated by the distance between M_6 and M_1 (~145 mm). The vertical angle of M_6, necessary to ensure the beam intersected the aperture of M_1, caused a small lateral offset between subsequent round trips. This offset was minimized during alignment (Supplementary Note 4). Round trips in the primary cavity generated the first 15 multiplexed beams, and a subsequent single-pass cavity (Extended Data Fig. 1b) increased the multiplicity to 30.

After the primary cavity (Extended Data Fig. 1a), the light was re-collimated by L_2. L_3 and L_4 formed a unitary magnification telescope that ensured that the lowest power beams were directed to the shallowest depths in the sample. The distances between M_6 and L_2, L_2 and L_3, and L_3 and L_4 were iteratively optimized in order to position the last beam exiting cavity A in the nominal focal plane of the objective, while maintaining as uniform as possible magnification for each beam. The beams were transmitted through a half-wave plate (HWP) and onto a polarizing beam splitter (PBS). The reflected portion of the beam underwent a single round trip through another custom-mirror-based 8-f re-imaging cavity (f = 250 mm, 2″ diameter, Layertec), before recombination with the transmitted portion of the beam (Extended Data Fig. 1b). The beams coupled to the secondary cavity were delayed an additional 6.7 ns, interleaving them in time with the beams transmitted by the PBS (Extended Data Fig. 1c). The focal planes of these delayed beams could be globally shifted by adjusting the position of M_9 and M_{11}, and formed two sub-volumes that were spatially contiguous, such that all 30 beams provided continuous sampling along the optical axis (Extended Data Fig. 1d). Manipulation of the HWP could be used to adjust the relative optical power of the sub-volumes in order to preserve matching to the scattering properties of the tissue. In total, 30 spatiotemporally multiplexed beams exited the secondary cavity, and the axial separation between imaging planes is ~16 μm, leading to a total axial sampling range of 465 μm.

Integration with mesoscope.

The output of the multiplexing module was interfaced with a commercial mesoscope (Thorlabs, Multiphoton Mesoscope)[18]. The mesoscope layout and accompanying electronics are shown in Extended Data Fig. 3. The configuration of the microscope followed normal operation conditions with the exception of some minor modifications. The remote focusing unit of the system, consisting of a PBS and objective mounting apparatus, was removed and replaced by a turning mirror to route beams directly to the first telescopic relay. This modification was necessary because light exiting MAxiMuM was split between two orthogonal polarization states and thus incompatible with the PBS in the remote focusing module. Furthermore, the axial range of MAxiMuM (~500 μm) makes remote focusing

redundant for our intended axial imaging range and thus an unnecessary drain on the power and dispersion compensation budgets.

Additionally, the electrical amplifier following the photo-multiplier tube (PMT) was removed, as the temporal response of the standard model amplifier used with the mesoscope was insufficient for multiplexed data. Given the power budget available from our custom laser source, we estimate that signals from each of the voxels in LBM can be up to about three times higher than those generated by a typical Ti:Sapphire laser (80 MHz, 2 W average power) coupled to the same mesoscope.

During mouse imaging experiments, typical signals consisted of ~250 counts/voxel, which, when considering the bit depth (12 bits), digitization range (2 V peak-to-peak), and impedance of our digitizer, corresponds to ~5 mA of photocurrent from the PMT. Given the sensitivity of the PMT (176 mA/W) and a gain of ~1×10^6, this suggests our signals are ~400 photons/voxel on average, with ~2 photons/voxel corresponding to dark counts. We can also estimate the photon number per voxel in a bottom-up fashion: assuming a 35 GM action cross-section and an intracellular concentration of 10 μM for GCaMP[52] and a total collection efficiency of ~10%[18], our signals are on the order of ~250 photons/voxel, in reasonable agreement with our top-down estimation accounting for background and auto-fluorescence.

Data acquisition.

Data were acquired using the commercial mesoscope-compatible version of the ScanImage software platform (Vidrio) with some additional customizations, as well as upgraded digitization hardware (Extended Data Fig. 3a). We used an evaluation board (Analog Devices, AD9516–0) to multiply a trigger signal from the OPCPA laser to 1,614 MHz, which in turn was fed to the upgraded digitizer (National Instruments, NI 5772) and field programmable gate array (FPGA, National Instruments, PXIe-7975R) to serve as a sample clock. This clock signal was used within the customized version of ScanImage to synchronize the line trigger to the pulse repetition rate of the laser, thus ensuring a single laser pulse constituted one voxel of the recording.

Additionally, the ScanImage customization allowed the user to define channels by integrating temporal windows of the raw PMT signal (Hamamatsu H11706–40) with respect to a trigger from the laser. The window for each channel was set to integrate the fluorescence signal associated with each beam from the MAxiMuM system such that the channels constitute the de-multiplexed axial planes of the volumetric recording (see channel plots in Extended Data Fig. 3b). The microscope recorded frames for each channel separately, in the same fashion as a two-color compatible microscope records separate channels from each PMT. Data streamed to disk consisted of 30 consecutive frames representing each channel, and thus each axial plane, repeated in sequence for each time point in the measurement.

Data processing.

Extended Data Fig. 5 shows a schematic of the data processing pipeline. Data recorded by the microscope were reassembled from constituent ROIs into 30 stacks of frames (x,y,t) corresponding to each plane of the volume which were each processed separately. Motion

correction of each plane was facilitated using the non-rigid version of the NoRMCorre algorithm[53] and neuronal footprints and time series were extracted with using the planar, patched version of the CaImAn software package[54,55]. Due to the reduced spatial sampling density of the data, the elliptical search method was found to most accurately extract neuronal signals from soma. The algorithm was initialized with a number of components dictated by the physiological expectation from the given volumetric field of view, assuming a standard density of 9.2×10^4 neurons per cubic millimeter[51,56]. The spatial correlation threshold was held at the default value of 0.4, and the minimum signal-to-noise parameter was set to 1.4. In practice, we found that this value was consistent with only keeping transients with statistically significant ($Z > 3\sigma$) transient activity (see statistics in the following section). Neuropil subtraction was facilitated using the global background feature of CaImAn with three components. Extended Data Fig. 6d shows example local neuropil traces (magenta lines) from neurons in the data set shown in Fig. 2 as well as the resultant traces after subtraction (black lines). Finally, neuronal footprints were screened using the 'mn' and 'mx' options in CaImAn such that components larger than the area expected for a 20 μm diameter neuron, or smaller than that of a 10 μm diameter neuron, in the equivalent pixel space, were eliminated.

The detected neurons from each plane in the volume were subsequently collated. The lateral positions of neuronal footprints were corrected for plane-to-plane offset using calibration values determined by recordings of pollen grains (Extended Data Fig. 4d). For cases where components in adjacent planes were temporally correlated above the default CaImAn threshold (0.8) and also had any spatially overlapping voxels, the time series and footprints were merged into a single component. First order moments in the x, y, and z directions were used to determine the centroids of each neuronal component. The field curvature imposed by the microscope was corrected using a parabolic profile with a −158 μm offset at the periphery of the full FOV[18].

Data analysis.

Correlations between neuronal activity and stimuli were analyzed by correlating the time series of each neuron with the corresponding stimulus vector, generated by convolving a time series composed of the onset of each stimulus or behavior with the expected kernel of the calcium indicator (see the final panel of Extended Data Fig. 5). This kernel had an exponential rise time of 200 ms and a decay of 550 ms, in agreement with the literature values for GCaMP6s[6]. All correlations considered between stimulus vectors and neuronal time series were Pearson type and used the raw time-series data rather than the deconvolved traces from CaImAn. The lag between the neuronal time series and each stimulus vector was defined as the time for which the cross-correlation between each trace and vector was maximized. For determining stimulus-tuned populations (Fig. 3b–d and Extended Data Fig. 9a–c), the median value of the distribution of lags was applied as an offset to each time series prior to determining correlation. For the temporal analysis in Fig. 3r,s, the relative lag values for each individual behavior-tuned neuron are shown with respect to the median lag value.

Null-hypothesis testing was conducted by creating a time series with a number of randomly shuffled ‘stimuli’ equal to the number presented during a typical recording. For uninstructed behaviors, shuffling was achieved by circulating each trace in the data set by a random value to remove temporal structure. The threshold for significant correlation with visual stimuli, whisker stimuli, or uninstructed animal behaviors was determined by fitting the shuffled correlations, r, to a normal distribution given by $p(r) = e^{-r^2/2\sigma^2}$. Correlations with stimuli for which $r > 3\sigma$ were considered highly correlated, while correlations below σ were deemed insignificant.

Hierarchical clustering was performed using Ward’s method with the Euclidean distance metric via the MATLAB function ‘linkage’. For the mixed representation analysis in Fig. 3j–o, the activity of each trial was defined as the integration of the time series of each neuron in a 5-second window following the presentation of the stimulus. Significance of the change in a neuron’s activity was determined with a t-test comparing the activity of all trials with the stimulus presented alone to those where the stimulus was presented coincidently with another stimulus. Neurons with $P < 0.05$ were considered to have significant change in activity.

Animal statistics and imaging power.

A total of $n = 6$ male and female animals transgenically expressing GCaMP6s in glutamatergic neurons (vGluT1-cre × fl-GCaMP6s, pCAG promoter, Jackson Labs stock numbers 031562 and 034422, respectively)[6,38], and $n = 3$ male and female animals expressing jGCaMP7f[42] through viral transfection were imaged during experiments. We used 150–200 mW of power to image with sufficient signal-to-noise ratio in jGCaMP7f-expressing mice, and 200–450 mW in transgenic animals with large (8 mm diameter) cranial windows. The power required for imaging is, at least partially, a function of the labeling strategy employed: Sparser labeling strategies (that is, those based on local viral injection, cell-type specific promoters, or other targeted labeling methods) result in less out-of-focus background fluorescence and thus higher SNR can be achieved for lower imaging power relative to imaging in animals for which denser labeling strategies (that is, transgenic labeling) are utilized. All imaging conditions used were determined to be within safe limits for brain heating through immunohistochemical labeling experiments and brain temperature simulations (Supplementary Note 5).

Extended Data Fig. 8b–d,h–j shows distributions of typical transient activity in GCaMP6s-expressing mice, including peak activity, baseline noise levels, and typical transient decay times. The characterizations are consistent with expectations for two-photon imaging. Extended Data Fig. 8d,j show the distributions of maximum Z-scores for the neuronal data sets shown in Figs. 2 and 5a. Z-scores were calculated by applying a three-point moving average to each neuron’s time series, finding the maximum value and normalizing by the baseline noise. The moving average in this instance ensures that we are measuring the robustness of all consecutive data points within the kernel of the indicator (200 ms rise time and 550 ms decay time for GCaMP6s sampled at a 4.7-Hz volume rate implies 3 samples within each transient) relative to noise, and not inflating the significance of isolated fluctuations in the data. At an SNR threshold of 1.4, the cutoff of the distribution is such

that neurons in the data set have activity exceeding at least three standard deviations of the baseline, indicating low likelihood of false-positive ROIs being classified as neurons. Extended Data Fig. 8f,k shows the distributions of nearest neighbor separations between neurons in the data set shown in Figs. 2 and 5a. The majority of pair-wise distances occur between 10 and 20 μm, in agreement with expectations for cortical neuronal density[51,56].

Apparatus for stimulus delivery and behavioral tracking.

Visual and somatosensory stimuli were controlled via a synchronization script running in parallel to ScanImage implemented on a microcontroller (Arduino Uno). A portion of the voltage used to open the laser shutter was read in by the microcontroller, triggering the beginning of a recording epoch and synchronizing the microcontroller clock to the ScanImage frame clock. For whisker stimulation, a motor shield and servo motor were used to move a brush forward and backward over the animals' whiskers at time intervals indicated by the stimulation protocol. The brush size and its proximity were chosen to stimulate all whiskers simultaneously (as opposed to stimulation of specific whiskers), and stimulation was applied contralaterally to the hemisphere being recorded by the microscope.

For visual stimuli, the microcontroller sent a 5 V TTL trigger signal to the control computer. A parallel MATLAB program read in these trigger signals and generated a series of images on a secondary external monitor (Waveshare 11.6′ LCD) placed ~20 cm from the animal's eyes. For each trigger signal, a 500-ms duration movie was displayed on the monitor consisting of a binary drifting grating pattern at the full dynamic range of the screen. The position of the screen was chosen to cover 72° of the animal's field of view horizontally and 43° vertically. The grating period was 0.07 cycles per degree, and the rate of drift was 1 cycle/second. The orientation of the grating followed a pattern of 0° (horizontal), 45°, 90° (vertical), and 135° and was repeated in this pattern for all stimuli during the recordings.

All rodents were head-fixed on a home-built treadmill with a rotation encoder affixed to the rear axle (Broadcom, HEDS-5540-A02) to measure the relative position of the tread during the recordings. Treadmill position, the microcontroller clock value, and the onset of either a visual or whisker stimulus were streamed to the control computer via a serial port connection and logged with a separate data logging script. The data logging script also triggered a camera (Logitech 860–000451) in order to capture additional animal behavior during recordings. Motion tracking of the rodent's left and right forelimbs and right hindlimb was facilitated using DeepLabCut[57,58]. An example recording of the animal with motion tracking super-imposed over top is shown in Supplementary Video 1. Stimulation was presented at 5-second intervals such that the calcium signal from correlated transients had sufficiently decayed before the onset of the next stimulus.

Data visualization.

All time-series data are displayed with a moving average corresponding to a 1-second time interval along the temporal axis to improve transient visibility. Calcium trace heatmaps are individually normalized to improve visualization. For 3D visualization, equally sized spheres in the data set were rendered using the 'scatter3' function in MATLAB. For Supplementary Videos 2, 8, and 10, the top ~57,000, ~33,000, and ~150,000 most active

neurons, respectively, are visualized and their time series are individually normalized, with the opacity of the representative sphere increasing with transient activity. For the volume projection images in Figs. 2a, 4d, and 5a in the manuscript, the top ~207,000, ~70,000, and ~266,000 most active neurons are rendered, respectively, and the color of each sphere represents the maximum projection of the corresponding neuron's time series with the color bar and opacity of each representative sphere adjusted for maximum visibility of the most active neurons.

Imaging power and immunohistochemical validation.

We used 150–200 mW of power to image FOVs of 0.6 × 0.6 × 0.5 mm with sufficient signal-to-noise ratio in jGCaMP7f-expressing mice. In transgenic mice, power was restricted to <250 mW in small FOVs (0.6 × 0.6 × 0.5 mm, 2 × 2 × 0.5 mm) to remain within previously established thresholds for brain safety. For large FOV recordings (3 × 5 × 0.5 mm, 5.4 × 6 × 0.5 mm), power ranged from 200 to 450 mW.

To further validate any possible neuropathological responses associated with these intensities and absolute power levels when delivered within the large volumetric FOVs and cranial windows, we employed immunohistochemical labeling. Brain sections were immunostained for the astrocyte activation marker GFAP following imaging under various laser intensities. All experiments were conducted at least 2 weeks after cranial window surgery. Awake head-fixed mice (wild-type) were subjected to various laser powers and scanning FOVs (Extended Data Fig. 10) for 9 minutes continuously at a depth of ~600 μm below the surface of the brain. For verification, we included a negative control condition corresponding to animals that had undergone cranial window implantation but had not been exposed to laser power in the region of the brain considered. As a positive control, we imaged with 360 mW of power in a FOV of 0.4 mm, exceeding previously established limits for brain safety[24]. To make full use of the 8 mm cranial window and each animal, both hemispheres of each mouse were used for separate experiments, with negative control and low exposure conditions contralateral to high exposure and positive control conditions. Sixteen hours after scanning, mice were deeply anaesthetized with isoflurane (4% flow rate of 0.5–0.7 l/minute) and transcardially perfused with cold phosphate-buffered saline (PBS) followed by 4% PFA (VWR International, 15710). Brains were extracted and placed in PFA for 24 hours and then transferred to 30% sucrose/PBS solution at 4 °C. Coronal sections (30-μm thickness) were collected from within and around the scanning FOV site using a cryostat (Leica Biosystems). Brain sections were permeabilized using 0.2% Triton X-100/PBS (PBST) for a 1-hour incubation period, followed by a blocking solution of 5% normal goat serum (NGS) in PBST for 1 hour. Sections were then incubated in primary mouse GFAP antibody (Protein Tech, 60190–1-Ig) (1:800) in PBST + 2% NGS for 24 hours at 4 °C. Sections were then washed 3 times with PBS for 20 minutes per wash, followed by an incubation period in Alexa-594-conjuagted goat anti-mouse antibody (Abcam, ab150116) (1:1,000) for 2 hours at room temperature. Sections were washed again 3 times with PBS for 20 minutes per wash with Hoechst 33342 (Invitrogen, H3570) (1:2,000) being added during the last wash, before being mounted on slides and coverslipped using anti-fade mounting medium (Invitrogen, P10144).

Brain sections were imaged at ×20 magnification using a resonant-scanning confocal microscope (Caliber I.D, RS-G4). Images were analyzed using FIJI. Relative fluorescence intensity was quantified by measuring the mean fluorescent intensity in a 1 × 1 mm axial area centered within the imaging FOV and dividing this measurement by the mean intensity of equivalently sized areas within the control hemispheres.

Brain heating simulations.

We used a finite difference model[59] to simulate laser-induced heating, thermal conductivity, and homeostatic cooling through blood perfusion. Additionally, we used modifications[60] to account for a scanned focal plane and heat conduction through the cranial window and immersion water. All simulations used an 8-mm cranial window, with the exception of those in Extended Data Fig. 10j, where the window size varies from 3 to 8 mm. The boundary conditions of the model were adjusted to assume a constant temperature of 25 °C at a distance 1.5 mm above the surface of the cranial window. We used a voxel size of 0.01 mm for light diffusion and 0.03 mm for heat diffusion, a time step of 0.16 ms and an optical wavelength of 960 nm. Material constants for glass and water were obtained from published tables.

Animal subjects and surgical procedures.

All surgical and experimental procedures were approved by the Institutional Animal Care and Use Committee of The Rockefeller University. Male and female adult C57BL/6J mice were supplied by Jackson Laboratory; VGlut-IRES-Cre × Ai162 crossed mice were bred in house. All mice were 28–70 days of age at the time of the first procedure, and were 49–291 days old during imaging experiments. Mice were allowed food and water ad libitum. In C57BL/6J mice, expression was achieved through injection of a genetically expressed calcium indicator adeno-associated virus (AAV9-syn-jGCaMP7f) at ~1–2 weeks prior to cranial window implantation following the procedure outlined in previous works[25].

During cranial window implantation, mice were anesthetized with isoflurane (1–1.5% maintenance at a flow rate of 0.7–0.9 l/min) and placed in a stereotaxic frame (RWD Life Science). The scalp was removed, and the underlying connective tissue was cleared from the skull. A custom-made stainless-steel head bar was fixed behind the occipital bone with cyanoacrylate glue (Loctite) and covered with black dental cement (Ortho-Jet, Lang Dental). For smaller windows, circular craniotomies (4-mm diameter) were performed over the desired imaging site. For larger windows, either a D-shaped single-hemisphere 4 × 8 mm craniotomy, or a circular 8 mm diameter dual-hemisphere craniotomy was performed. A ~1 mm segment of the skull furthest posterior within the bounds of the diameter of the craniotomy was kept intact to avoid the junction of the sagittal and transverse sinus vessels while drilling. A circular 4 mm or 8 mm glass coverslip, or a D-shaped 4 × 8 mm glass coverslip, with 1 mm of the bottom removed (#1 thickness, Warner Instruments) was implanted in the craniotomy site and sealed in place with tissue adhesive (Vetbond). The exposed skull surrounding the cranial window was covered with a layer of cyanoacrylate glue and then dental cement. Post-operative care consisted of 3 days of subcutaneous delivery of meloxicam (0.125 mg/kg), antibiotic-containing feed (LabDiet no. 58T7), and meloxicam-containing (0.125 mg/tablet) food supplements (Bio-Serv no. MD275-M). After

surgery, animals were returned to their home cages and were given at least one week for recovery before being subjected to imaging experiments. Mice with damaged dura or unclear windows were euthanized and were not used for imaging experiments.

Reporting Summary.

Further information on research design is available in the Nature Research Reporting Summary linked to this article.

Data availability

The raw image data presented in this work is currently too large for sharing via typical public repositories. It is available from the corresponding author upon reasonable request. Source data are provided with this paper.

Code availability

Stimulus delivery and treadmill control was implemented with a combination of MATLAB, Python, and Arduino scripts. Neuronal segmentation and non-rigid motion correction were based on the CaImAn[53,54] and NoRMCorre[52] software packages, respectively, and implemented using MATLAB. All custom code, including pipelines based on CaImAn and NoRMCorre, is publicly available on the Vaziri lab GitHub repository (https://github.com/vazirilab).

Extended Data

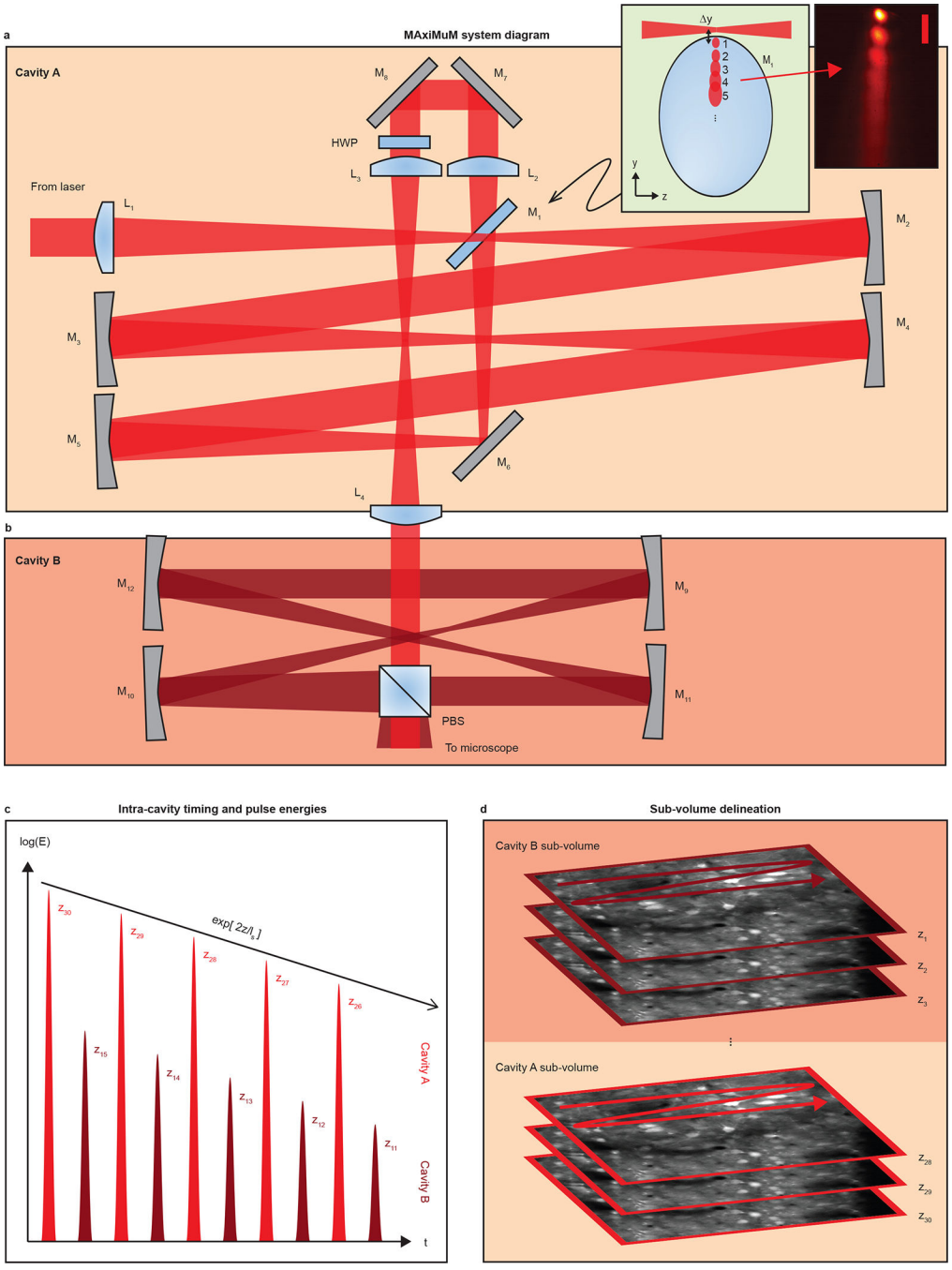

Extended Data Fig. 1 |. Full schematic of MAxiMuM.

a, Primary cavity schematic, where 'Ms' denote mirrors, 'Ls' denote lenses, and 'HWP' denotes a half-wave plate. Insets show a schematic of M_1 in the *Y-Z* plane illustrating that the beam entering the cavity passes over top of M_1, while subsequent beams encounter M_1 and a camera image of the first ~7 beams exiting the cavity just after M_1. **b**, A second cavity with shorter focal length mirrors creates a copy of the 15 pulses from Cavity A and shifts

them in time and axial location to achieve the full 30 beams and 465 μm axial range of the MAxiMuM system. **c**, Temporal schematic of pulses from cavity A and B. Due to the shorter delay of cavity B relative to A, the pulse trains are interleaved. The pulse energies for each beam decrease exponentially due to the partially transmissive mirror (M_1) in cavity A. exponential decrease is matched to the expected scattering length (l_s) for brain tissue (~200 μm). power levels for cavity B pulses are lower than those from A since cavity B pulses are sent to more superficial layers in the brain; relative power can be controlled by the HWP in **a**. **d**, Sub-volume schematic. Cavities A and B form two sub-volumes, with the planes from cavity A below those from B such that together they continuously sample the entire axial range.

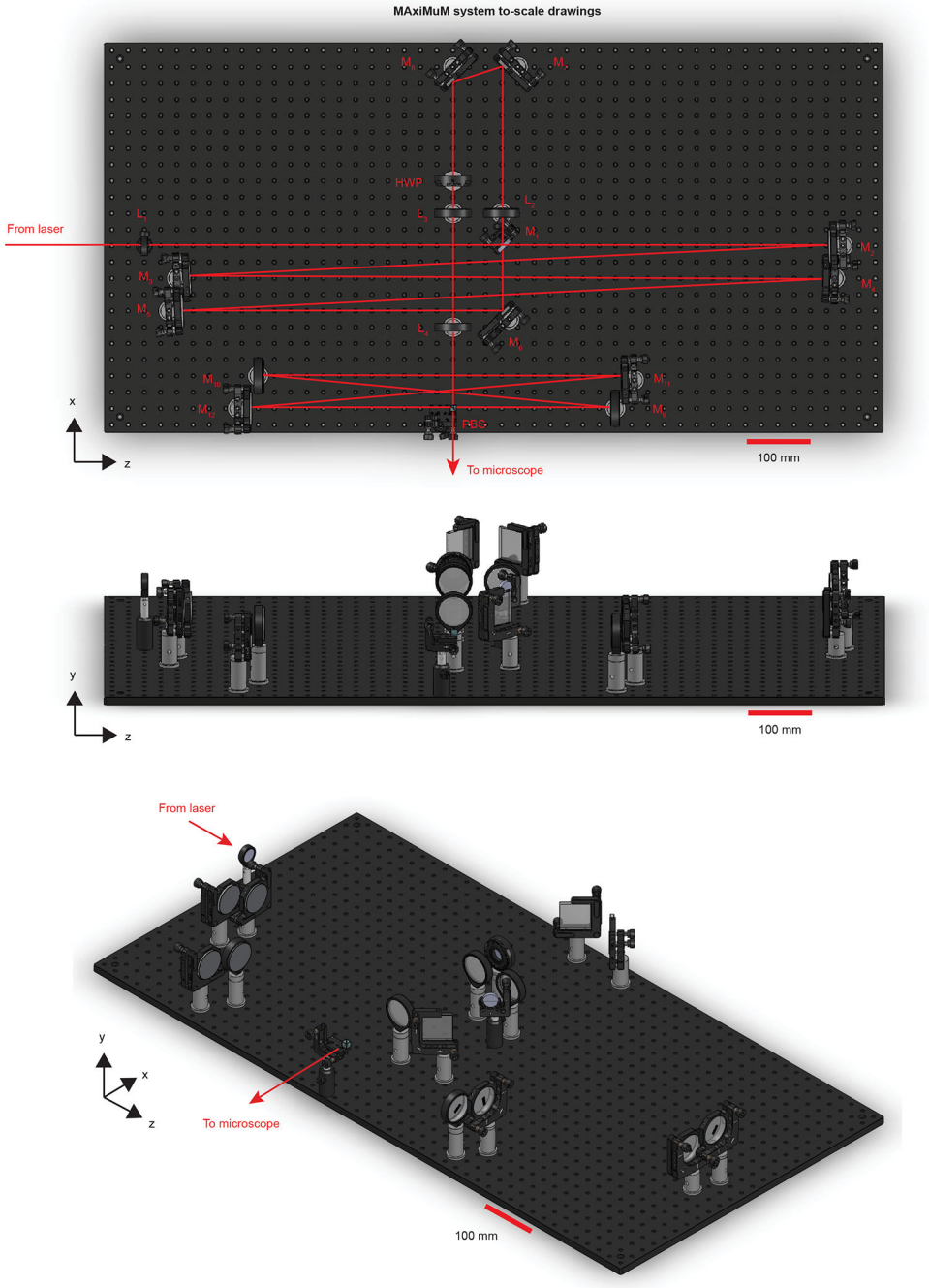

Extended Data Fig. 2 |. CAD drawings of the MAxiMuM system.
Scale bars: 100 mm.

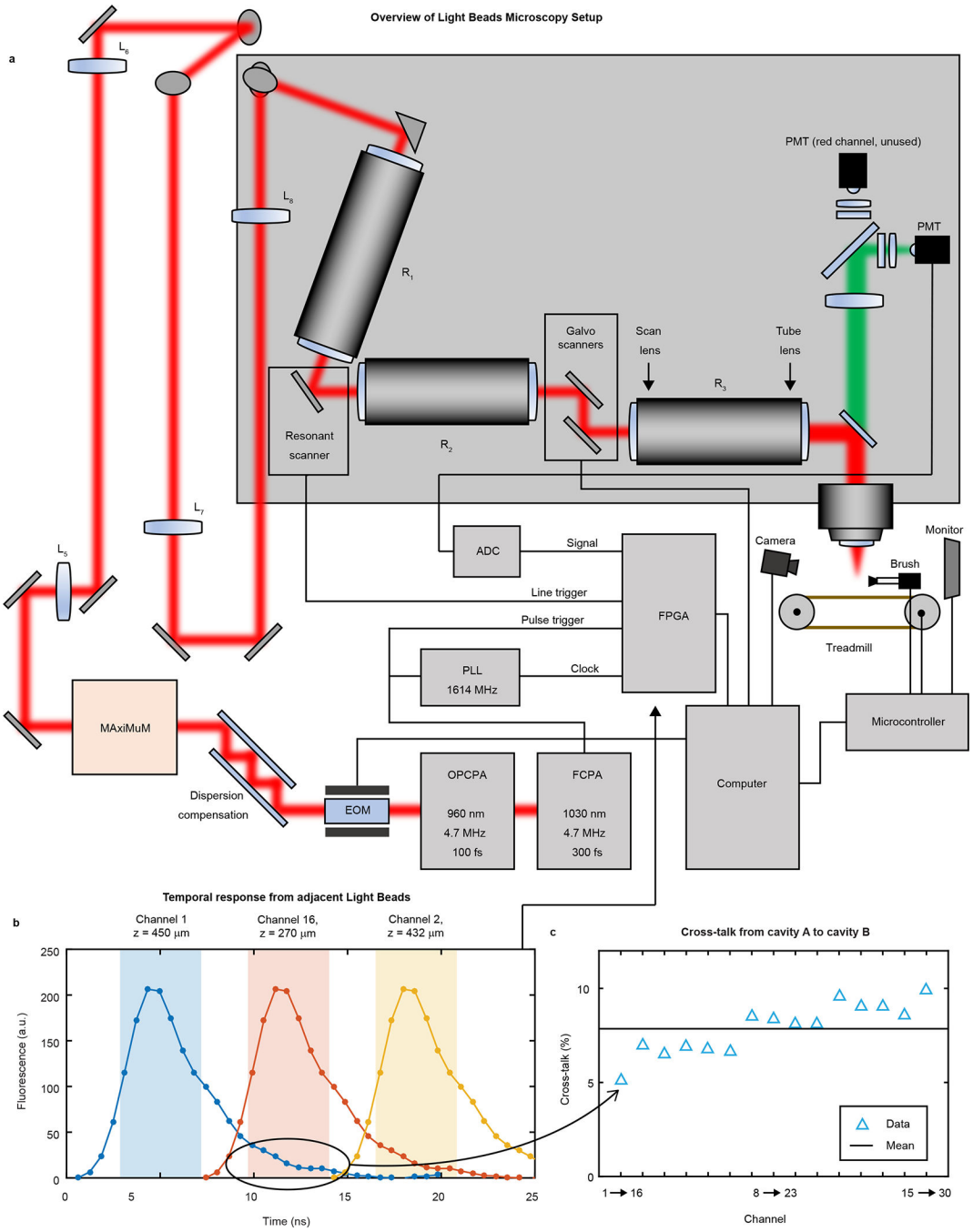

Extended Data Fig. 3 |. Full microscope schematic.

a, Setup schematic for mesoscope system starting from the fiber chirped-pulse amplifier (FCpA), through the optical parametric chirped-pulse amplifier (OPCPA), electro-optic modulator (EOM), dispersion compensation path, MAxiMuM, and into the microscope. ‘Ls’ denote lenses, ‘Rs’ denote relay lens pairs, ‘PMT’ denotes photo-multiplier tube, ‘ADC’ denotes analog to digital converter, and ‘PLL’ denotes phase-locked loop. **b**, Schematic showing channel allocation for demultiplexing of signal from three adjacent light beads on the FPGA. Data points are the measured impulse response for fluorescence from GCaMP6f

measured with our PMT and associated electronics, captured with 1614 MHz (0.62 ns) resolution. Shaded regions denote the integration boundaries for each de-multiplexed channel. **c**, Measurement of crosstalk of channels 1—15 into channels 16—30 (that is Cavity A → Cavity B). Black horizontal line shows mean value at ~7%.

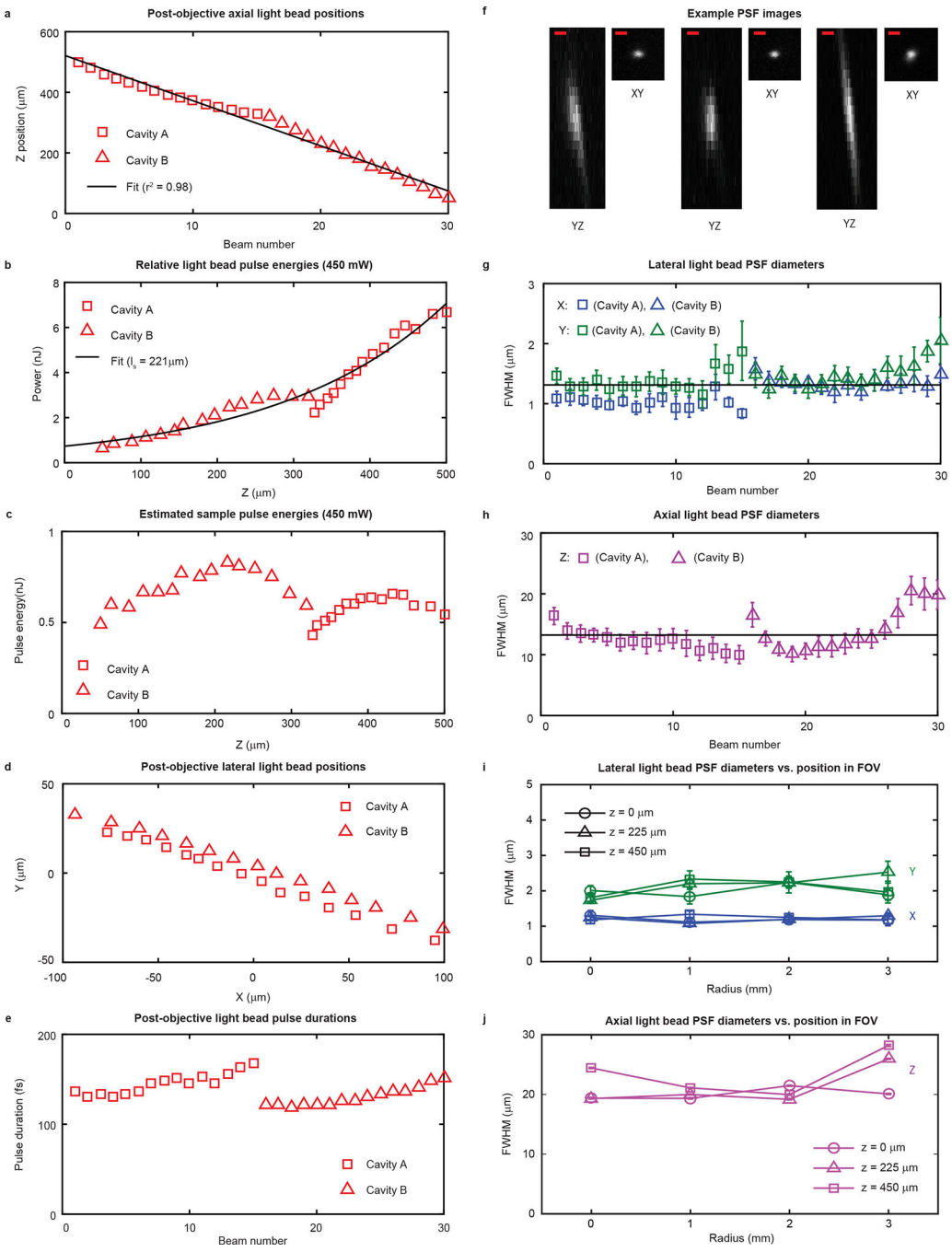

Extended Data Fig. 4 |. Post-objective calibration of light bead columns generated by MAxiMuM.

a–d, Axial position (**a**), estimated pulse energy out of the objective (**b**) and in the sample (**c**), and transverse position of the light beads from MAxiMuM (**d**), calibrated by translating

a pollen grain through the focus of the microscope. estimated pulse energies assume 450 mW average power and a scattering length of 200 μm. **e**, Pulse duration measurements of each beam from MAxiMuM, post-objective. **f-j**, characterization of light bead point-spread functions. **f**, example images of PSFs for light beads 5, 15, and 25 in the *x,y* and *x,z* planes. Scale bar: 2 μm **g**, Lateral point-spread function full-width at half-maximum diameters for each light bead. mean value shown by horizontal black line. error bars denote the 95% confidence interval values for the Gaussian fits used to determine PSF widths. **h**, Axial point-spread function full-width at half-maximum diameters for each light bead. mean value shown by horizontal black line. error bars denote the 95% confidence interval values for the Lorentzian fits used to determine PSF widths**. i, j** Point-spread function FWHM lateral and axial widths, respectively, for the top (z = 0 μm, bead 30), middle (z = 225 μm, bead 18) and bottom (z = 450 μm, bead 1), of the light bead column as a function of radial position in the FOV.

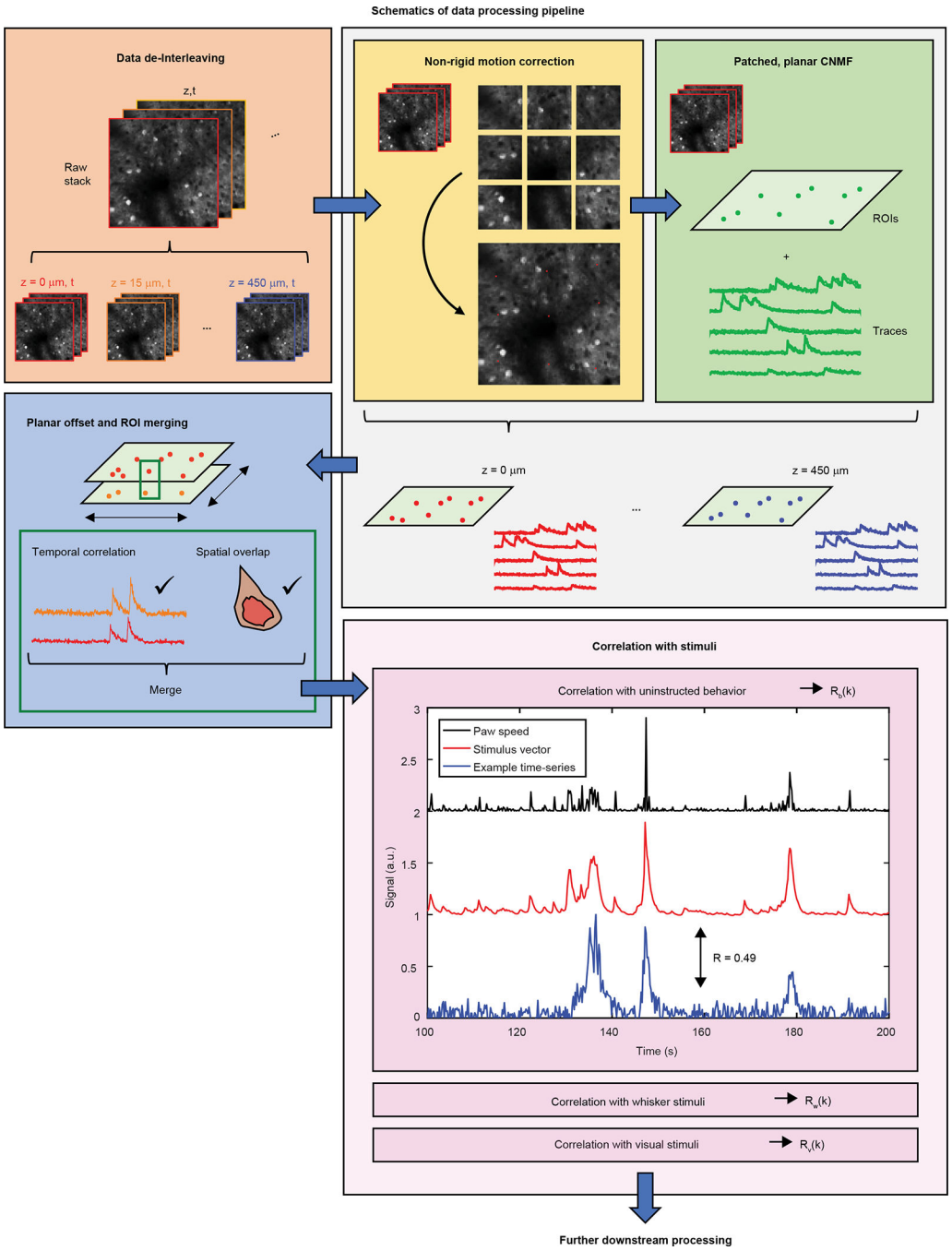

Extended Data Fig. 5 |. schematic of the data processing pipeline.

Raw data is assembled into frames and separated into individual temporal stacks for each *z* plane. each stack is separately motion-corrected and sent through a constrained non-negative matrix factorization (CNMF) sub-routine to extract neuronal footprints and time-series. Lateral offsets between the planes are accounted for using calibration values, and neurons with both correlated temporal activity and overlapping spatial footprints are merged to prevent doubly-counted cells. Neurons are correlated with vectors representing each stimulus to determine if they are tuned. example raw and kernel-convolved stimulus

vectors and an example time-series for a tuned neuron are shown for uninstructed behaviors during a recording.

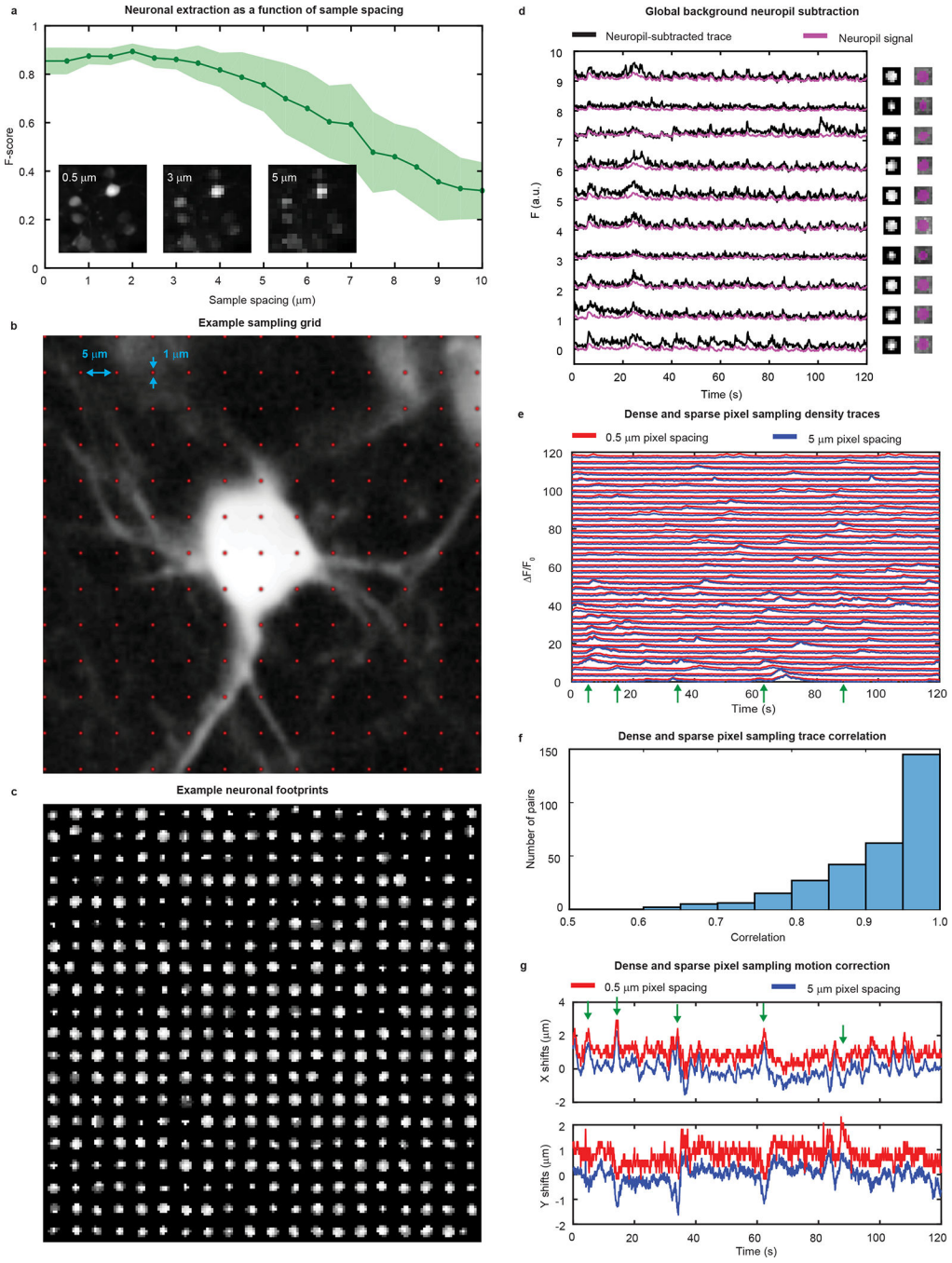

Extended Data Fig. 6 |. Data fidelity and validation in the sparse sampling regime.

a, Extraction fidelity, measured by F-score, as a function of sample spacing. F-score is defined as the harmonic mean of the sensitivity and precision of the neuronal extraction. Solid line indicates mean value, shaded region indicates one standard deviation from the mean. example images for 0.5, 3, and 5 μm sample spacing inset. **b**, To-scale schematic

of a sparse sampling grid (5 μm sample-to-sample spacing) with a 1 μm FWHM PSF over an example soma. **c**, 400 example footprints extracted from the data set shown in Fig. 2 with our data processing pipeline. **d**, Example traces showing the neuropil subtraction mechanism: In-plane signal around each neuronal footprint (left column) is used to estimate the background in the region overlapping the cell body (rightmost column, magenta overlay) and contamination of the extracted transients due to surrounding neuropil. The obtained neuropil signal (magenta lines) is then subtracted from the raw transient signal to result in decontaminated traces (black lines). **e**, Example traces extracted from a densely sampled (0.5 μm sampling) ground truth data set (red lines) compared to traces extracted from the same data set with intentional down-sampling to reflect the sparse sampling condition (5 μm sampling, blue lines); traces are intentionally offset by $2 \times \Delta F/F_0$ for clarity. **f**, Correlation between traces extracted from 7 ground truth data sets and traces extracted from down-sampled copies of the same data sets, indicating strong correlation ($r = 0.91 \pm 0.11$)**. g**, Comparison of the pixel shifts predicted by our motion correction algorithm for an example ground truth data set (red line) and the same data set after intentional down-sampling (blue line); traces are intentionally offset by 1 μm for clarity. pixel shift estimates are not affected by the down-sampling.

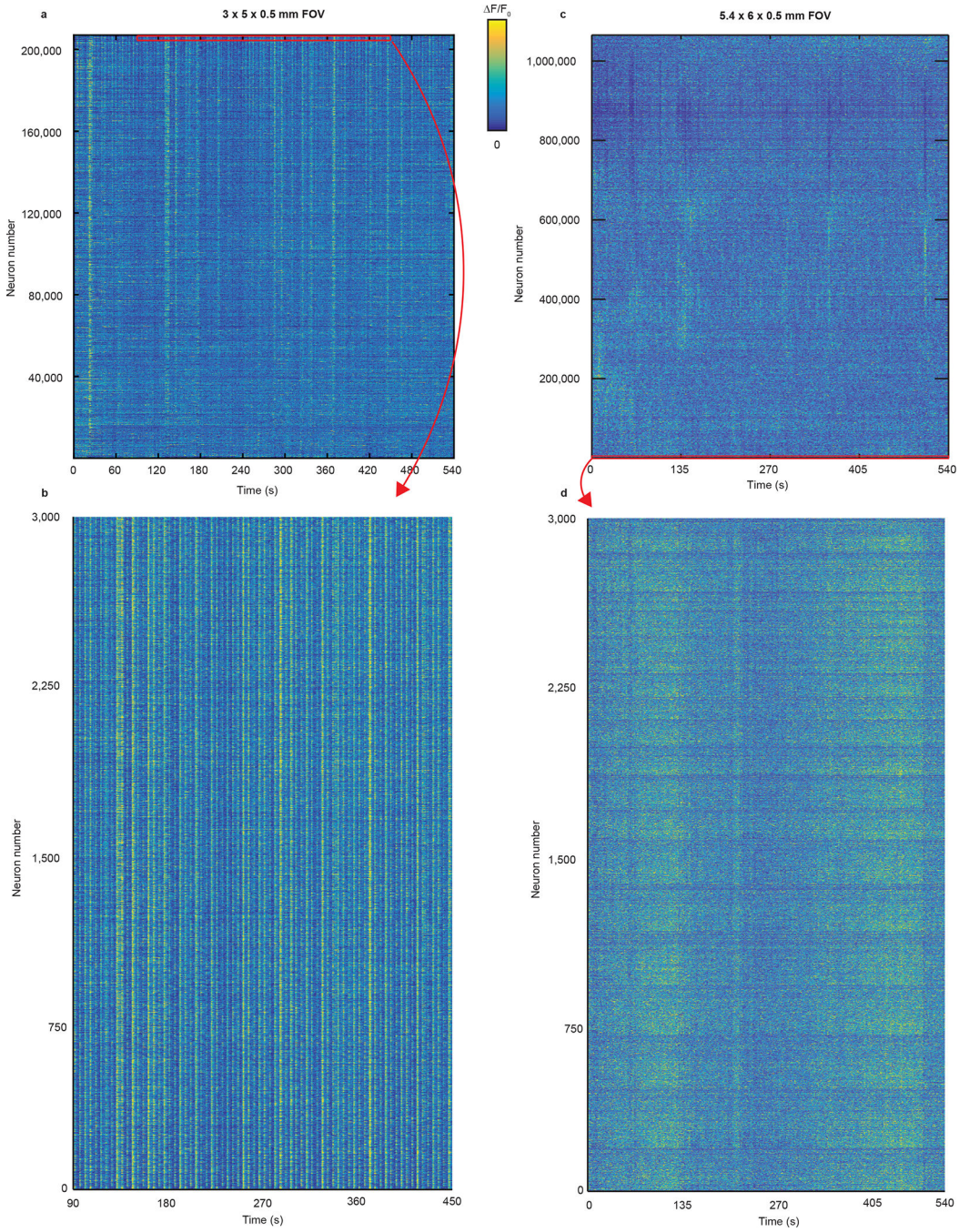

Extended Data Fig. 7 |. Normalized heatmaps of extracted neuronal activity.

a, Heatmap of 207,030 neurons extracted from the data set shown in Fig. 2a recorded in a 3 × 5 × 0.5 mm FOV at 4.7 Hz. **b**, A high resolution subset of 3,000 neurons from the population shown in **a**. **c**, Heatmap of 1,065,289 neurons extracted from the data set shown in Fig. 5a recorded in a 5.4 × 6 × 0.5 mm FOV at 2.2. **d**, A high resolution subset of 3,000 neurons from the population shown in **c**.

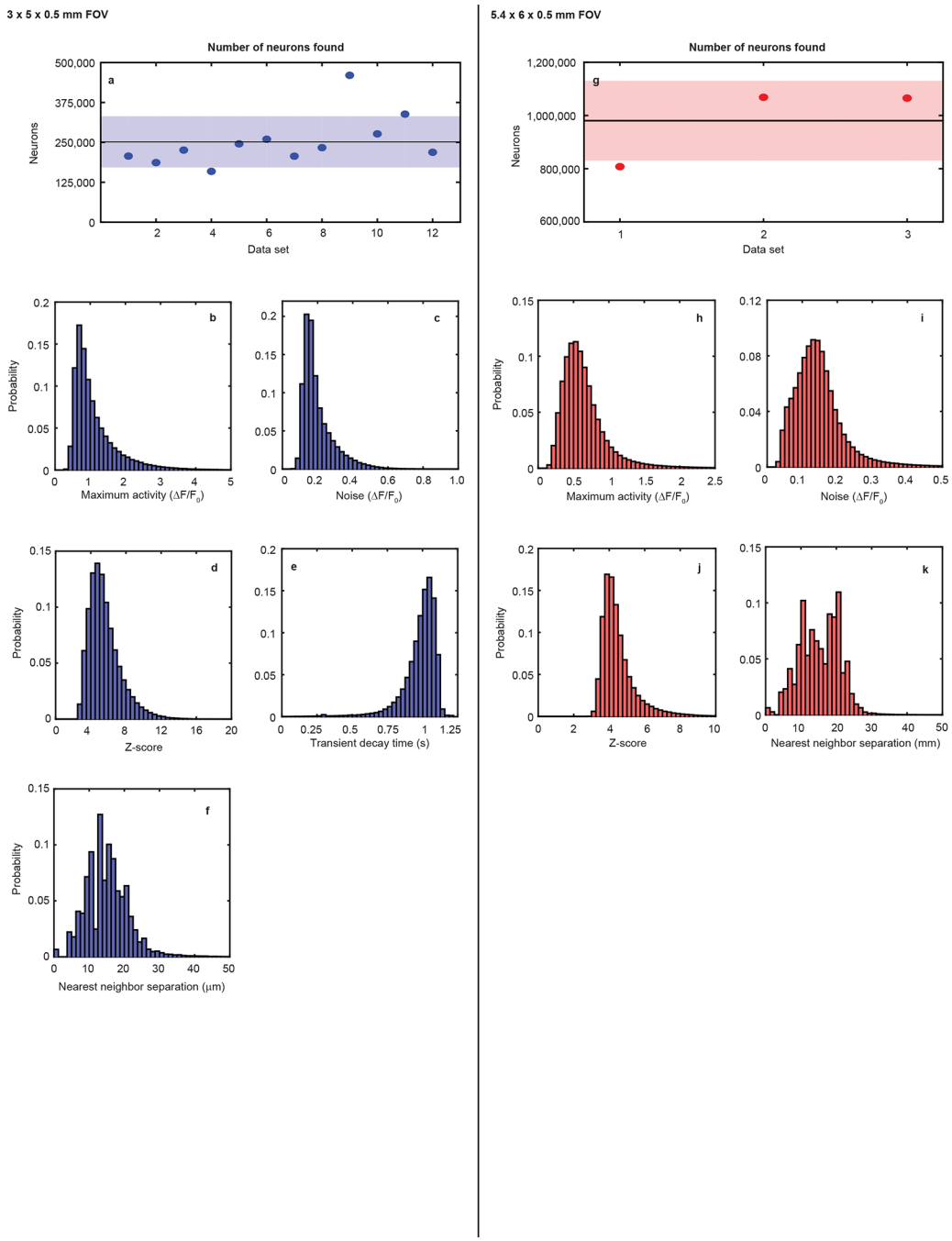

Extended Data Fig. 8 |. Indicator and extraction statistics.

a, Summary of the number of neurons extracted from 12 recordings with ~3 × 5 × 0.5 mm FOV across $N = 6$ animals; solid black line denotes the mean, shaded region denotes 1 standard deviation from the mean; data set 1 corresponds to the recording shown in Figs. 2 and 3. **b,c,d,e,f** Distribution of maximum $\Delta F/F_0$ values, baseline noise levels, Z-scores, and transient decay times for transients measured in mice expressing GCaMP6s from the experiment shown in Fig. 2. **g**, Summary of the number of neurons extracted from 3 recordings with ~5.4 × 6 × 0.5 mm FOV across $N = 3$ animals; solid black line denotes

the mean, shaded region denotes 1 standard deviation from the mean; dataset 1 corresponds to the recording shown in Fig. 5a. **h,i,j,k** Distributions quantifying neuronal activity for transients extracted from Fig. 5a, following those in **b-f**.

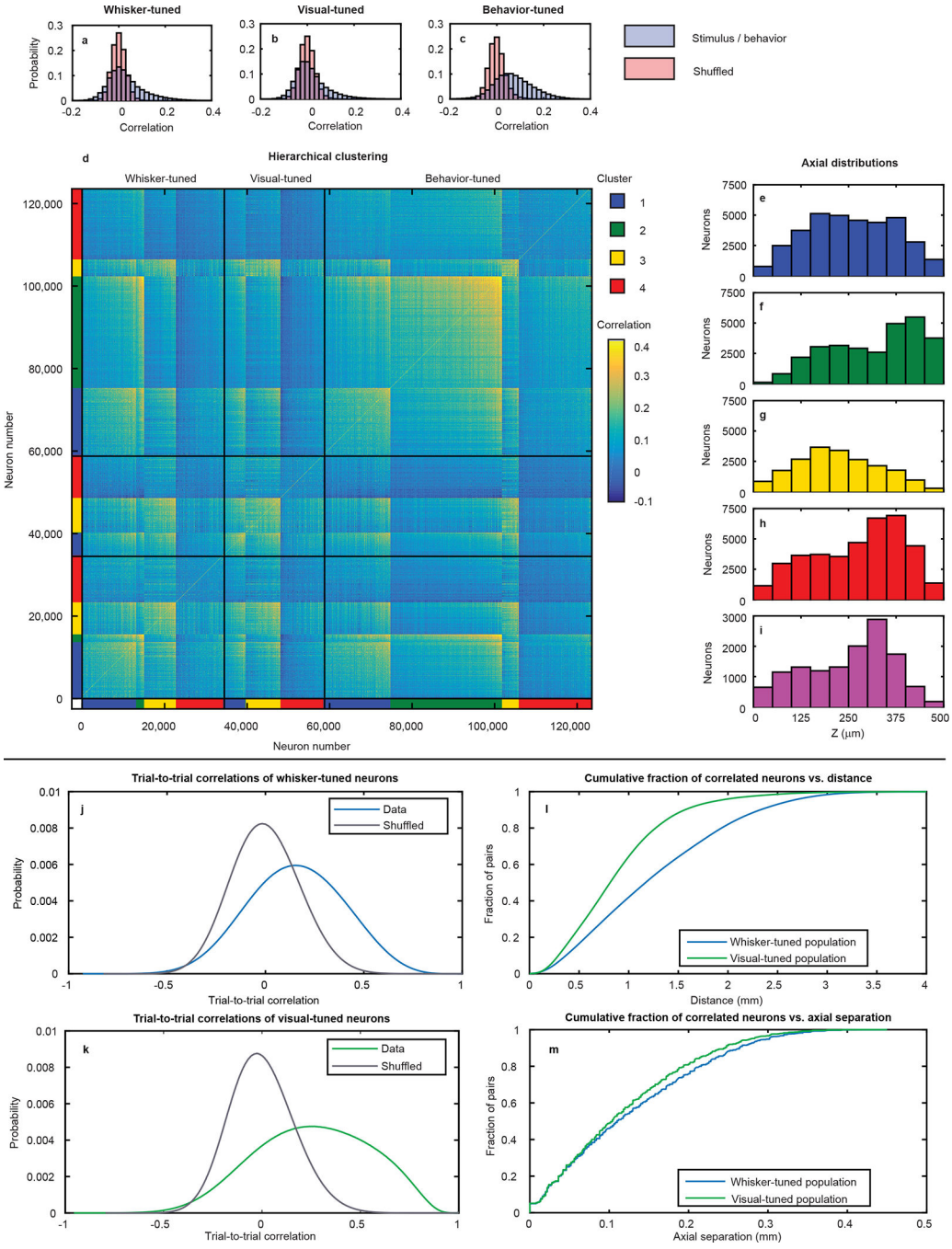

Extended Data Fig. 9 |. Hierarchical clustering and trial-to-trial variability analysis of stimulus-tuned neurons from the dataset shown in Fig. 2.

a–c, Correlation distributions of neurons with whisker stimuli, visual stimuli, and uninstructed spontaneous animal behaviors (blue), compared to time-shuffled distributions (red). **d**, Correlation matrix of all neurons tuned to any stimulus condition. The matrix

is sorted by stimulus (boundaries denoted by black lines), cluster, and mean Pearson correlation. **e–i**, Axial spatial distributions of neurons in clusters 1 through 4 and the uncorrelated population, respectively. **j**, Distribution of the correlation between trial-to-trial responses of pairs of whisker-tuned neurons compared to a distribution where trial order was randomly shuffled. **k**, Equivalent distributions to those shown in **j** for visual-tuned neurons. **l**, Cumulative fraction of significantly covarying ($R > 3\sigma$, Pearson correlation) pairs of neurons as a function of neuron-to-neuron separation. **m**, Cumulative fraction of significantly covarying ($R > 3\sigma$, Pearson correlation) pairs of neurons as a function of neuron-to-neuron axial separation.

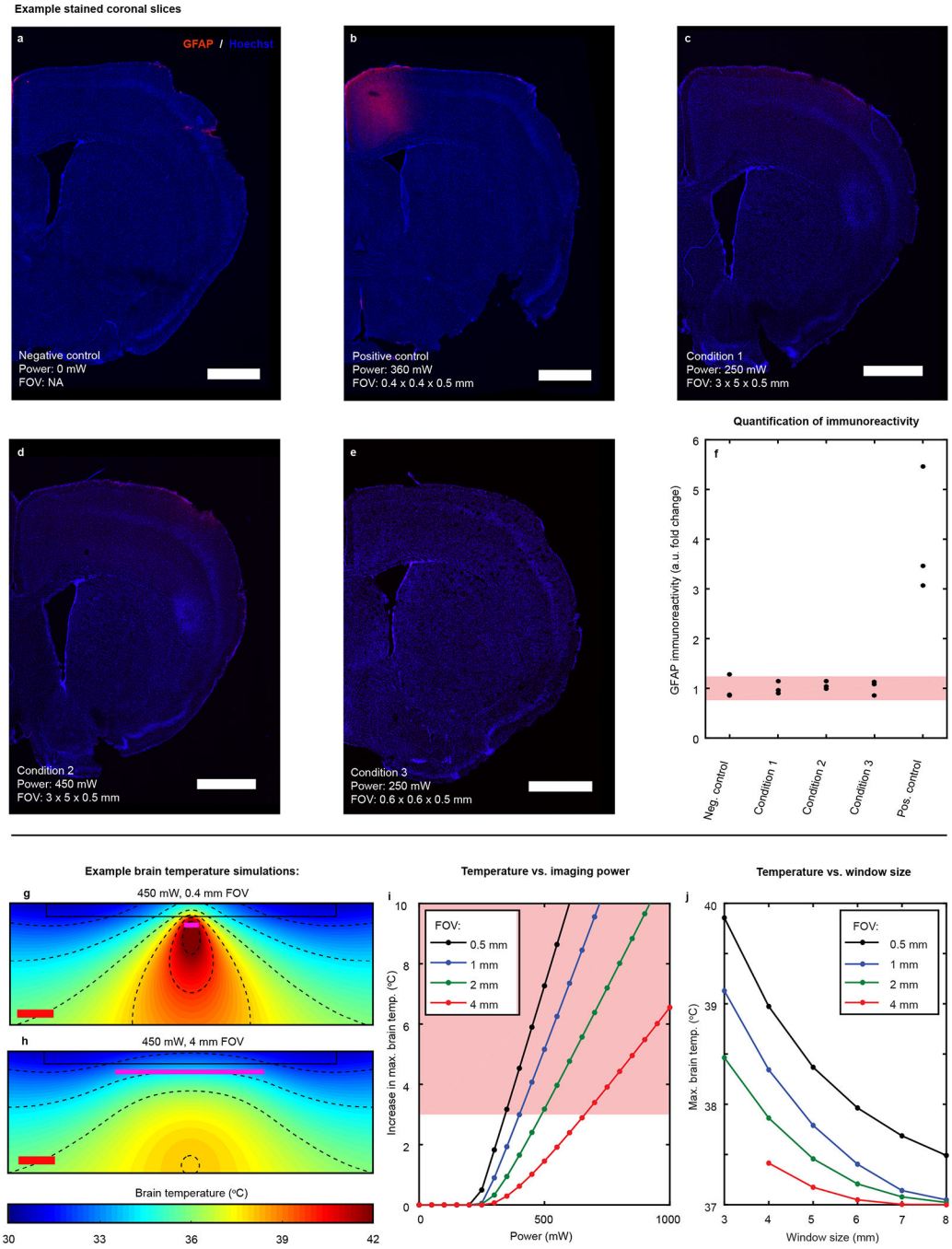

Extended Data Fig. 10 |. Brain heating experimental data and simulations.

a-e, Representative images of brain sections showing immunolabeling for astrocyte activation marker (anti-GFAP, red) and DNA stain (Hoechst 33342, blue) after exposure to the laser power and FOV listed below. Scale bars: 1 mm **a**, control, no laser exposure. **b**, 360 mW, 0.4 × 0.4 × 0.5 mm FOV (2250 mW/mm^2). **c**, 250 mW, 3 × 5 × 0.5 mm FOV (17 mW/mm^2). **d**, 450 mW, 3 × 5 × 0.5 mm FOV (34 mW/mm^2). **e**, 250 mW, 0.6 × 0.6 × 0.5 mm FOV (700 mW/mm^2). **f**, Intensity of immunolabeling corresponding to imaging intensity as a fraction compared to mean of control samples. $N = 3$ separate brain

hemispheres per condition. Shaded area denotes the 95% confidence interval of the control group mean. **g,h**, Simulations of brain temperature at steady state for 450 mW of optical power in a (**g**) 0.4 mm FOV and a (**h**) 4 mm FOV; magenta lines indicated nominal focal plane; scale bars: 1 mm. Brain temperature in **g** heats to ~6 °C above core temperature (37 °C), while heating in **h** is only ~1 °C. Solid black lines denote boundaries of the cranial window, magenta lines indicate focal plane, dashed black lines indicate contours separated by 2 °C. Scale bar: 1 mm. **i**, Maximum brain temperature as a function of optical power and FOV. Cooling of the brain through the cranial window leads to a minimum power threshold before the onset of heating in the brain. **j**, Brain temperature for a fixed power level (250 mW) as a function of cranial window diameter and FOV. Larger cranial windows lead to less overall heating of the brain.

Supplementary Material

Refer to Web version on PubMed Central for supplementary material.

Acknowledgements

We thank P. Strogies and J. M. Petrillo (Precision Instrumentation Technology, Rockefeller University) for manufacturing mechanical components and K. Cialowicz (Bio-Imaging Resource Center, Rockefeller University) for performing confocal imaging of immunolabelled samples. We thank S. Weisenburger (LUMICKS) for helpful discussions related to microscope development and synchronization, and T. Nöbauer (Rockefeller University) for discussions regarding data management and processing. We thank K. Podgorski (Howard Hughes Medical Institute) for sharing previously used simulation software[58] for laser-induced heating. Research reported in this publication was supported by the National Institute of Neurological Disorders and Stroke of the National Institutes of Health under award numbers 5U01NS103488, 1RF1NS113251, and 1RF1NS110501 (A. V.) and the Kavli Foundation (A.V., J. M., J. D.). This research was supported in part by a Bristol-Myers Squibb Postdoctoral Fellowship (J. D.).

References

1. Denk W, Strickler JH & Webb WW Two-photon laser scanning fluorescence microscopy. Science 248, 73–76 (1990). [PubMed: 2321027]
2. So PTC, Dong CY, Masters BR & Berland KM Two photon excitation fluorescence microscopy. Annu. Rev. Biomed. Eng. 2, 399–429 (2000). [PubMed: 11701518]
3. Helmchen F & Denk W Deep tissue two-photon microscopy. Nat. Methods 2, 932–940 (2005). [PubMed: 16299478]
4. Miyawaki A et al. Fluorescent indicators for Ca^{2+} based on green fluorescent proteins and calmodulin. Nature 388, 882–887 (1997). [PubMed: 9278050]
5. Nakai J, Ohkura M & Imoto K A high signal-to-noise Ca^{2+} probe composed of a single green fluorescent protein. Nat. Biotechnol. 19, 137–141 (2001). [PubMed: 11175727]
6. Chen T et al. Ultrasensitive fluorescent proteins for imaging neuronal activity. Nature 499, 295–300 (2013). [PubMed: 23868258]
7. Harris JA et al. Hierarchical organization of cortical and thalamic connectivity. Nature 575, 195–202 (2019). [PubMed: 31666704]
8. Kuchibhotla KV et al. Parallel processing by cortical inhibition enables context-dependent behavior. Nat. Neurosci. 20, 62–71 (2017). [PubMed: 27798631]
9. Stringer C, Pachitariu M, Steinmetz N, Carandini M & Harris KD High-dimensional geometry of population responses in visual cortex. Nature 571, 361–365 (2019). [PubMed: 31243367]
10. Rumyantsev OI et al. Fundamental bounds on the fidelity of sensory cortical coding. Nature 580, 100–105 (2020). NC. [PubMed: 32238928]

11. Musall S, Kaufman MT, Juavinett AL, Gluf S & Churchland AK Single-trial neural dynamics are dominated by richly varied movements. Nat. Neurosci. 22, 1677–1686 (2019). NC. [PubMed: 31551604]
12. Makino H et al. Transformation of cortex-wide emergent properties during motor learning. Neuron 94, 880–890 (2017). [PubMed: 28521138]
13. Mao T et al. Long-range neuronal circuits underlying the interaction between sensory and motor cortex. Neuron 71, 111–123 (2011).
14. Pinto L et al. Task-dependent changes in the large-scale dynamics and necessity of cortical regions. Neuron 104, 810–8214 (2019). [PubMed: 31564591]
15. Lin Q et al. Cerebellar neurodynamics predict decision timing and outcome on the Single-Trial level. Cell 180, 1–16 (2020). [PubMed: 31836194]
16. Bartolo R, Saunders RC, Mitz AR & Averbeck BB Information-limiting correlations in large neural populations. J. Neurosci. 40, 1668–1678 (2020). [PubMed: 31941667]
17. Tsai PS et al. Ultra-large field-of-view two-photon microscopy. Opt. Express 23, 13833–13847 (2015). [PubMed: 26072755]
18. Sofroniew NJ, Flickinger D, King J & Svoboda K A large field of view two-photon mesoscope with subcellular resolution for in vivo imaging. eLife 5, 14472 (2016).
19. Stirman JN, Smith IT, Kudenov MW & Smith SL Wide field-of-view, multi-region, two-photon imaging of neuronal activity in the mammalian brain. Nat. Biotechnol. 34, 857–862 (2016). [PubMed: 27347754]
20. Ji N, Freeman J & Smith SL Technologies for imaging neural activity in large volumes. Nat. Neurosci. 19, 1154–1164 (2016). [PubMed: 27571194]
21. Weisenburger S & Vaziri A A guide to emerging technologies for large-scale and whole-brain optical imaging of neuronal activity. Annu. Rev. Neurosci. 41, 431–452 (2018). [PubMed: 29709208]
22. Yang W & Yuste R In vivo imaging of neural activity. Nat. Methods 14, 349–359 (2017). [PubMed: 28362436]
23. Yu C, Stirman JN, Riichiro Hira YY, & Smith SL Diesel2p mesoscope with dual independent scan engines for flexible capture of dynamics in distributed neural circuitry. Preprint at bioRxiv 10.1101/2020.09.20.305508 (2020).
24. Prevedel R et al. Fast volumetric calcium imaging across multiple cortical layers using sculpted light. Nat. Methods 13, 1021–1028 (2016). [PubMed: 27798612]
25. Weisenburger S et al. Volumetric Ca^{2+} imaging in the mouse brain using hybrid multiplexed sculpted light (HyMS) microscopy. Cell 177, 1–17 (2019). [PubMed: 30901532]
26. Kazemipour A et al. Kilohertz frame-rate two-photon tomography. Nat. Methods 16, 778–786 (2019). [PubMed: 31363222]
27. Botcherby EJ, Juškaitis R & Wilson T Scanning two photon fluorescence microscopy with extended depth of field. Opt. Commun. 268, 253–260 (2006).
28. Song A et al. Volumetric two-photon imaging of neurons using stereoscopy (vTwINS). Nat. Methods 14, 420–426 (2017). [PubMed: 28319111]
29. Lu R et al. Rapid mesoscale volumetric imaging of neural activity with synaptic resolution. Nat. Methods 17, 291–294 (2020). [PubMed: 32123393]
30. Zhang T et al. Kilohertz two-photon brain imaging in awake mice. Nat. Methods 16, 1119–1122 (2019). [PubMed: 31659327]
31. Tsai Y-H et al. Two-photon microscopy at >500 volumes/second. Preprint at bioRxiv 10.1101/2020.10.21.349712 (2020).
32. Amir W et al. Simultaneous imaging of multiple focal planes using a two-photon scanning microscope. Opt. Lett. 32, 1731–1733 (2007). [PubMed: 17572762]
33. Cheng A, Gonçalves J, Golshani P, Arisaka K & Portera-Cailliau C Simultaneous two-photon calcium imaging at different depths with spatiotemporal multiplexing. Nat. Methods 8, 139–142 (2011). [PubMed: 21217749]
34. Tsyboulski D et al. Remote focusing system for simultaneous dual-plane mesoscopic multiphoton imaging. Preprint at bioRxiv 10.1101/503052 (2018).

35. Wu J et al. Ultrafast laser-scanning time-stretch imaging at visible wavelengths. Light.: Sci. Appl. 6, e16196 (2017). [PubMed: 30167195]
36. Beaulieu DR, Davison IG, Kılıç K, Bifano TG & Mertz J Simultaneous multiplane imaging with reverberation two-photon microscopy. Nat. Methods 17, 283–286 (2020). [PubMed: 32042186]
37. Wu J et al. Kilohertz two-photon fluorescence microscopy imaging of neural activity in vivo. Nat. Methods 17, 287–290 (2020). [PubMed: 32123392]
38. Daigle TL et al. A suite of transgenic driver and reporter mouse lines with enhanced brain-cell-type targeting and functionality. Cell 174, 465–480 (2018). [PubMed: 30007418]
39. Horton N et al. In vivo three-photon microscopy of subcortical structures within an intact mouse brain. Nat. Photon 7, 205–209 (2013).
40. Cooper BG, Manka TF & Mizumori SJY Finding your way in the dark: the retrosplenial cortex contributes to spatial memory and navigation without visual cues. Behav. Neurosci. 115, 1012–1028 (2001). [PubMed: 11584914]
41. Cohen MR & Kohn A Measuring and interpreting neuronal correlations. Nat. Neurosci. 14, 811–819 (2011). [PubMed: 21709677]
42. Stringer C et al. Spontaneous behaviors drive multidimensional, brainwide activity. Science 364, 255 (2019). [PubMed: 31000656]
43. Dana H et al. High-performance calcium sensors for imaging activity in neuronal populations and microcompartments. Nat. Methods 16, 649–657 (2019). [PubMed: 31209382]
44. Rigotti M et al. The importance of mixed selectivity in complex cognitive tasks. Nature 497, 585–590 (2013). [PubMed: 23685452]
45. Abbott LF & Dayan P The effect of correlated variability on the accuracy of a population code. Neural Comput. 11, 91–101 (1999). NC. [PubMed: 9950724]
46. Steinmetz NA, Zatka-Haas P, Carandini M & Harris KD Distributed coding of choice, action and engagement across the mouse brain. Nature 576, 266–273 (2019). [PubMed: 31776518]
47. Runyan C, Piasini E, Panzeri S & Harvey CD Distinct timescales of population coding across cortex. Nature 548, 92–96 (2017). [PubMed: 28723889]
48. Li N, Daie K, Svoboda K & Druckmann S Robust neuronal dynamics in premotor cortex during motor planning. Nature 532, 459–464 (2016). [PubMed: 27074502]
49. Howe MW & Dombeck DA Rapid signalling in distinct dopaminergic axons during locomotion and reward. Nature 535, 505–510 (2016). [PubMed: 27398617]
50. Rajasethupathy P et al. Projections from neocortex mediate top-down control of memory retrieval. Nature 526, 653–659 (2015). [PubMed: 26436451]
51. Lau C et al. Exploration and visualization of gene expression with neuroanatomy in the adult mouse brain. BMC Bioinf. 9, 153–163 (2008).

References

52. Zariwala HA et al. A Cre-dependent GCaMP3 reporter mouse for neuronal imaging in vivo. J. Neuroscience 32, 3131–3141 (2012).
53. Pnevmatikakis EA & Giovannucci A NoRMCorre: an online algorithm for piecewise rigid motion correction of calcium imaging data. J. Neurosci. Meth. 291, 83–94 (2016).
54. Pnevmatikakis EA et al. Simultaneous denoising, deconvolution, and demixing of calcium imaging data. Neuron 89, 285–299 (2016). [PubMed: 26774160]
55. Giovannucci A et al. CaImAn: an open source tool for scalable calcium imaging data analysis. eLife 8, 38173 (2019).
56. Kandel ER, Schwartz JH & Jessell TM Principles of Neural Science. (McGraw-Hill, Health Professions Division, 2000).
57. Mathis A et al. DeepLabCut: markerless pose estimation of user-defined body parts with deep learning. Nat. Neurosci. 21, 1281–1289 (2018). [PubMed: 30127430]
58. Nath T et al. Using DeepLabCut for 3D markerless pose estimation across species and behaviors. Nat. Protoc. 14, 2152–2176 (2019). [PubMed: 31227823]

59. Stujenske JM, Spellman T & Gordon JA Modeling the spatiotemporal dynamics of light and heat propagation for in vivo optogenetics. Cell Rep. 12, 525–534 (2015). [PubMed: 26166563]

60. Podgorski K & Ranganathan G Brain heating induced by near-infrared lasers during multiphoton microscopy. J. Neurophysiol. 116, 1012–1023 (2016). [PubMed: 27281749]

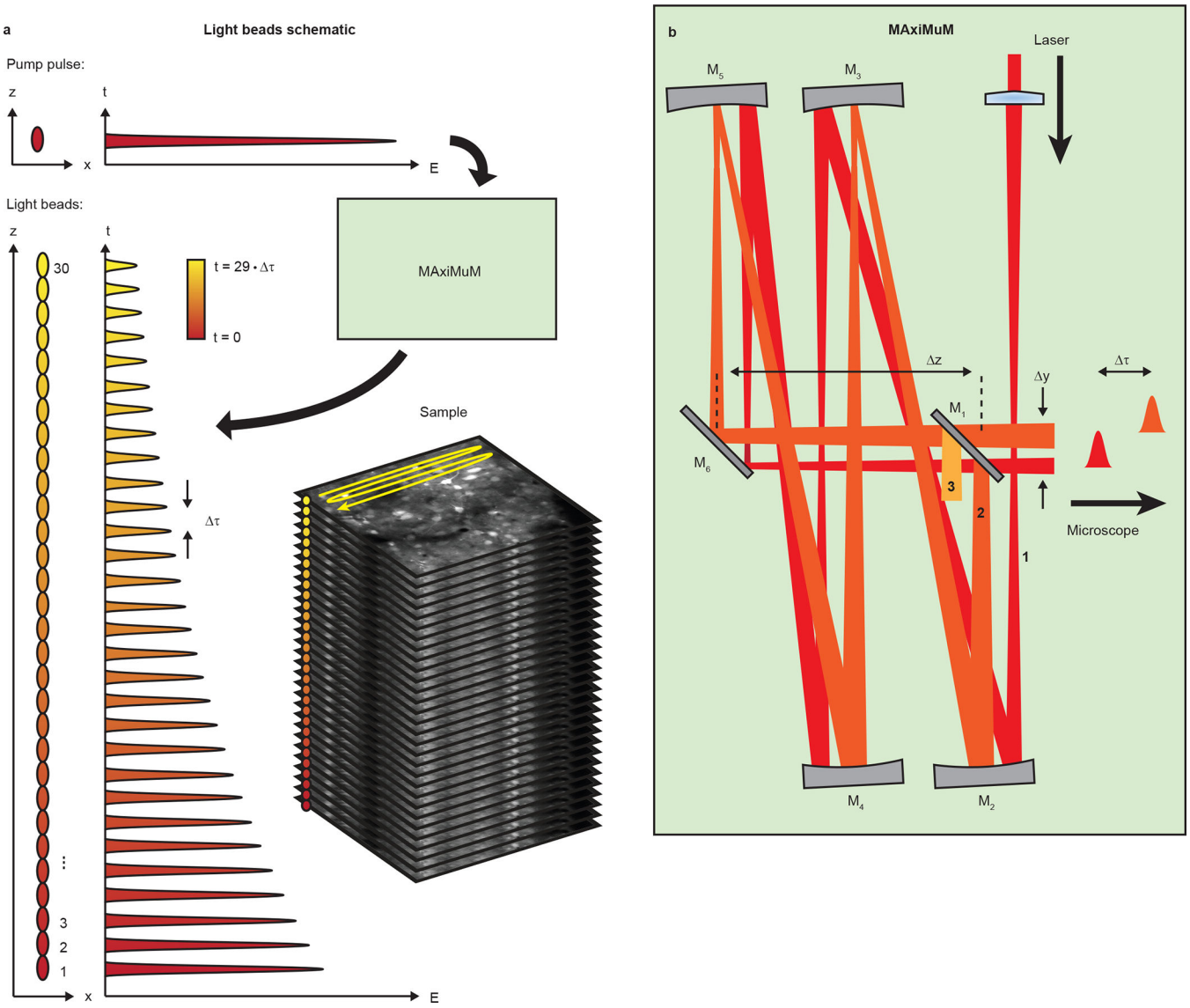

Fig. 1 |. LBM schematics.

a, An ultrafast pump pulse is split into 30 copies, which are delayed in time and focused into different depths in the sample, forming a column of 'light beads.' The column of foci is thus sampling the entire volume scanned at the nominal frame-rate of the microscope. each bead is temporally distinct, allowing time-binned decoding of its fluorescence and the plane from within the volume from where it was emitted. **b**, MAxiMuM schematic. The red beam represents light entering the cavity, formed by four concave mirrors (M_1–M_4). A partially transmissive mirror (PRM) reinjects most of the light back into the cavity. Beams accumulate an axial offset (Δz) and a temporal offset ($\Delta \tau$) for each round trip, forming a column of light beads.

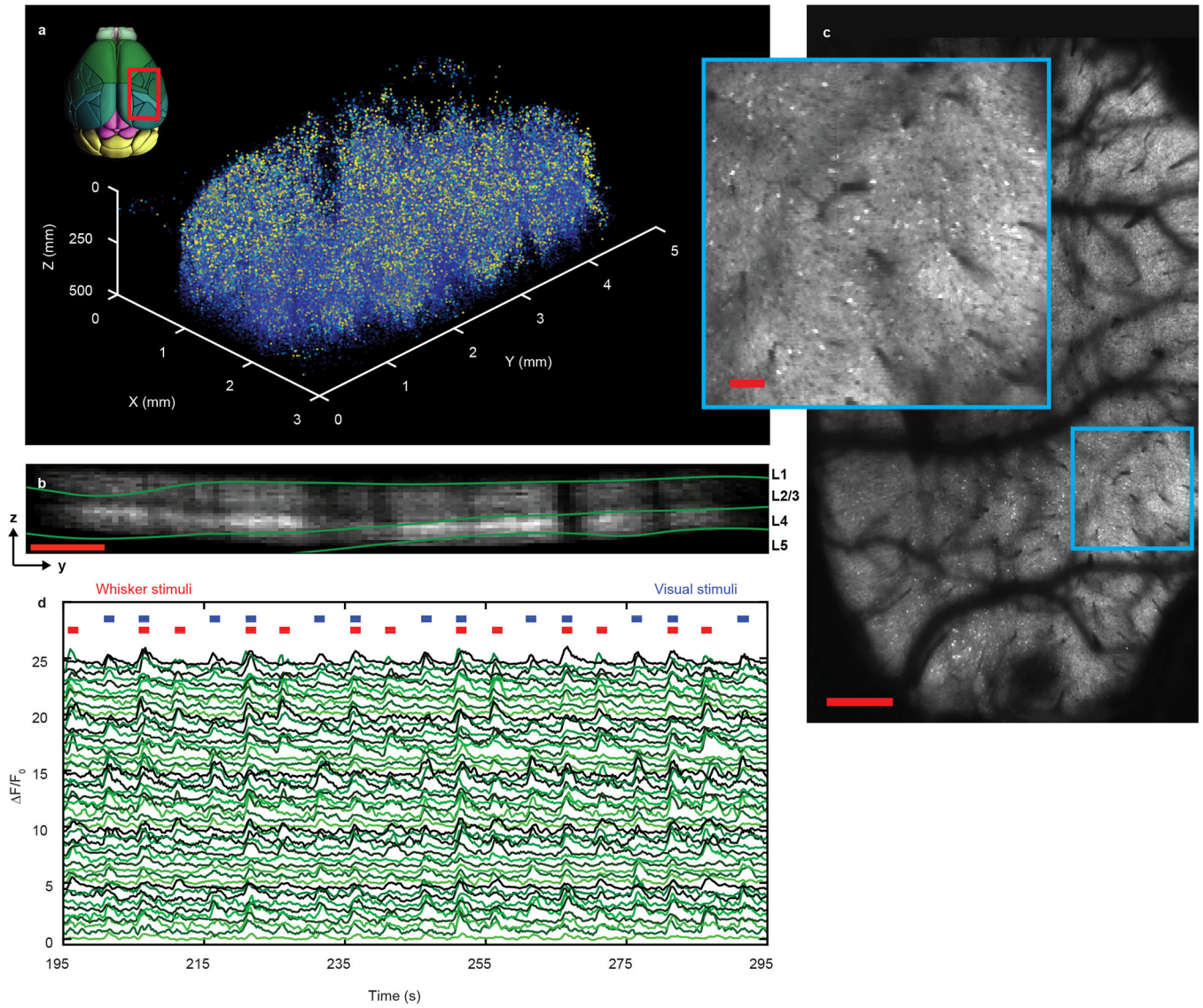

Fig. 2 |. recording of 207,030 neurons at 4.7-Hz rate within a volume of ~3 × 5 × 0.5 mm in the cortex of a GCaMP6s-expressing mouse during whisker and visual stimulation.

a, Three-dimensional (3D) rendering of extracted neuron spatial coordinates and maximum projected activity for a 9-minute recording. The transverse brain image reproduced from the Allen Brain Atlas, Brain explorer 2 (ref. [51]). **b**, *Y*–*Z* projection of the neuron density. Approximate boundaries between cortical layers are denoted with green lines. All depth values are displayed relative to the pia. **c**, mean projection image from the recording in **a** at 344 μm depth; scale bar, 250 μm. Inset, zoomed in boxed region of **c**; scale bar, 100 μm. **d**, Subset of 50 example traces with whisker and visual stimuli denoted by red and blue markers, respectively. Offset, 0.5 × $\Delta F/F_0$.

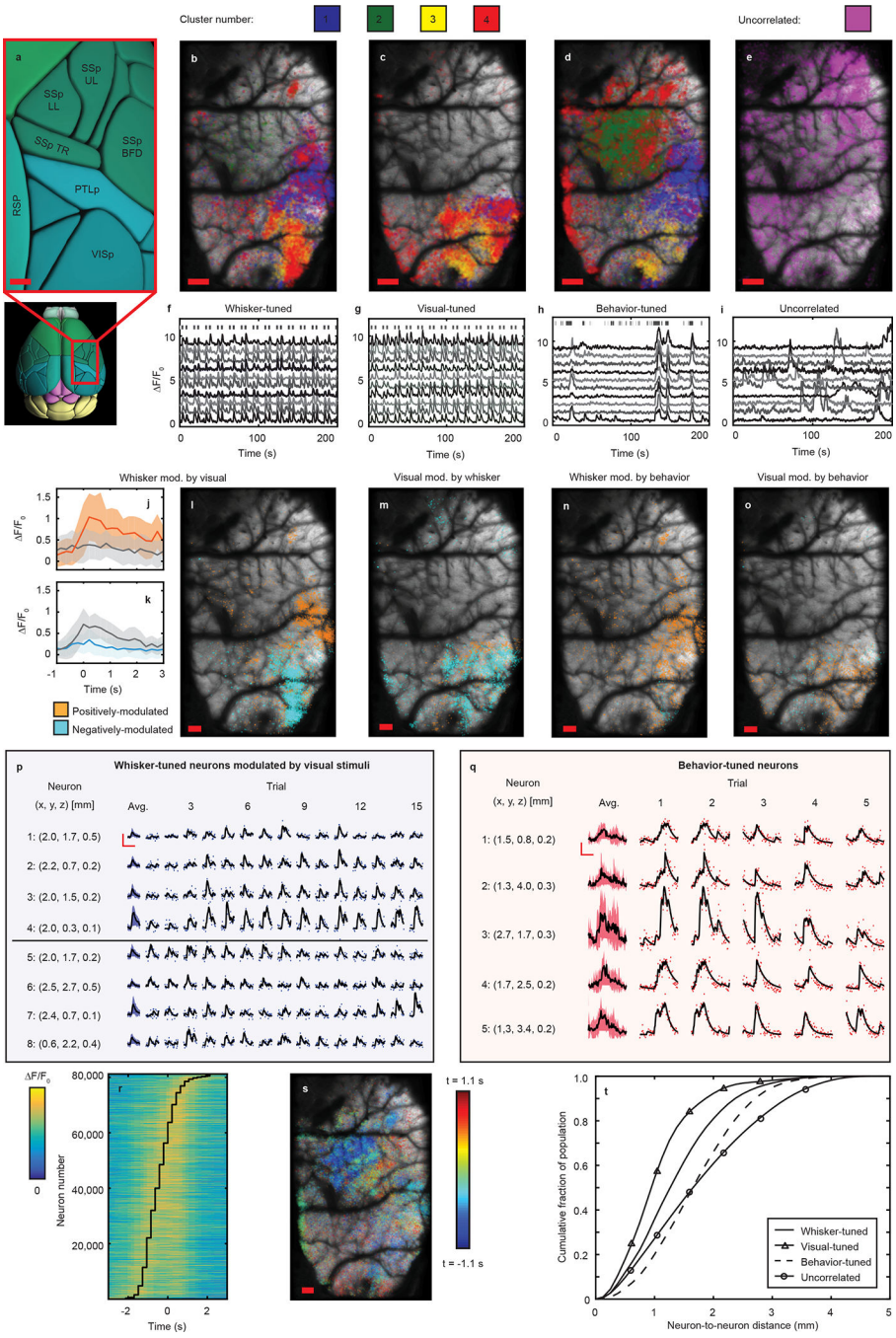

Fig. 3 |. Analysis of the activity of stimulus-tuned and behavior-correlated neurons in a single-hemisphere recording.

a, Brain regions covered by the recording in Fig. 2, reproduced from the Allen Brain Atlas, Brain explorer 2 (ref. [51]). Scale bar, 250 μm. **b–e**, Transverse spatial distributions of neurons tuned to a single stimulus condition. The correlation matrix for all tuned neurons was hierarchically clustered, generating four clusters colored in blue, green, yellow, and red. maps correspond to whisker stimuli (**b**), visual stimuli (**c**), or behaviors (**d**), or a population of neurons not correlated with any stimuli (**e**). Scale bars, 250 μm. **f–i**, example neuronal

traces from populations tuned to whisker stimuli (**f**), visual stimuli (**g**), or spontaneous behaviors (**h**), or that were uncorrelated (**i**). Occurrence of stimuli denoted by markers in **f–h**. Offset, 1.0 × $\Delta F/F_0$. **j**,**k**, Trial-averaged activity of example whisker-tuned neurons with (orange in **j**, cyan in **k**) and without (gray) the presence of a simultaneous visual trial. Solid lines denote mean of all trials, shaded regions denote 1 s.d. from mean. **l**, Lateral spatial distributions of the orange and cyan populations in **j** and **k**. Scale bar, 250 μm. **m**,**n**,**o**, Lateral spatial distributions of visually tuned neurons modulated by simultaneous whisker stimuli (**m**), whisker-tuned neurons modulated by simultaneous animal behaviors (**n**), and visually tuned neurons modulated by simultaneous animal behaviors (**o**). **p**,**q**, Single-trial activity, for example neurons tuned to whisker stimuli for trials with simultaneous visual stimuli (**p**) and neurons tuned to spontaneous animal behaviors (**q**). Shaded regions denote 1 s.d. from the mean. Raw data are shown by markers, and black lines denote the deconvolved response. Horizontal and vertical scale bars, 1.0 × $\Delta F/F_0$, 5 seconds. **r**, Heat map of trial-averaged activity of behavior-tuned neurons with relative lag denoted by the overlaid black line. **s**, Lateral spatial distribution of behavior-tuned neurons color-coded by relative lag. Scale bar, 250 μm. **t**, Cumulative fraction of populations tuned to a given condition (whisker stimulus, visual stimulus, spontaneous behavior, uncorrelated) with significant mutual correlation ($R > 3\sigma$) captured within a given neuron-to-neuron separation.

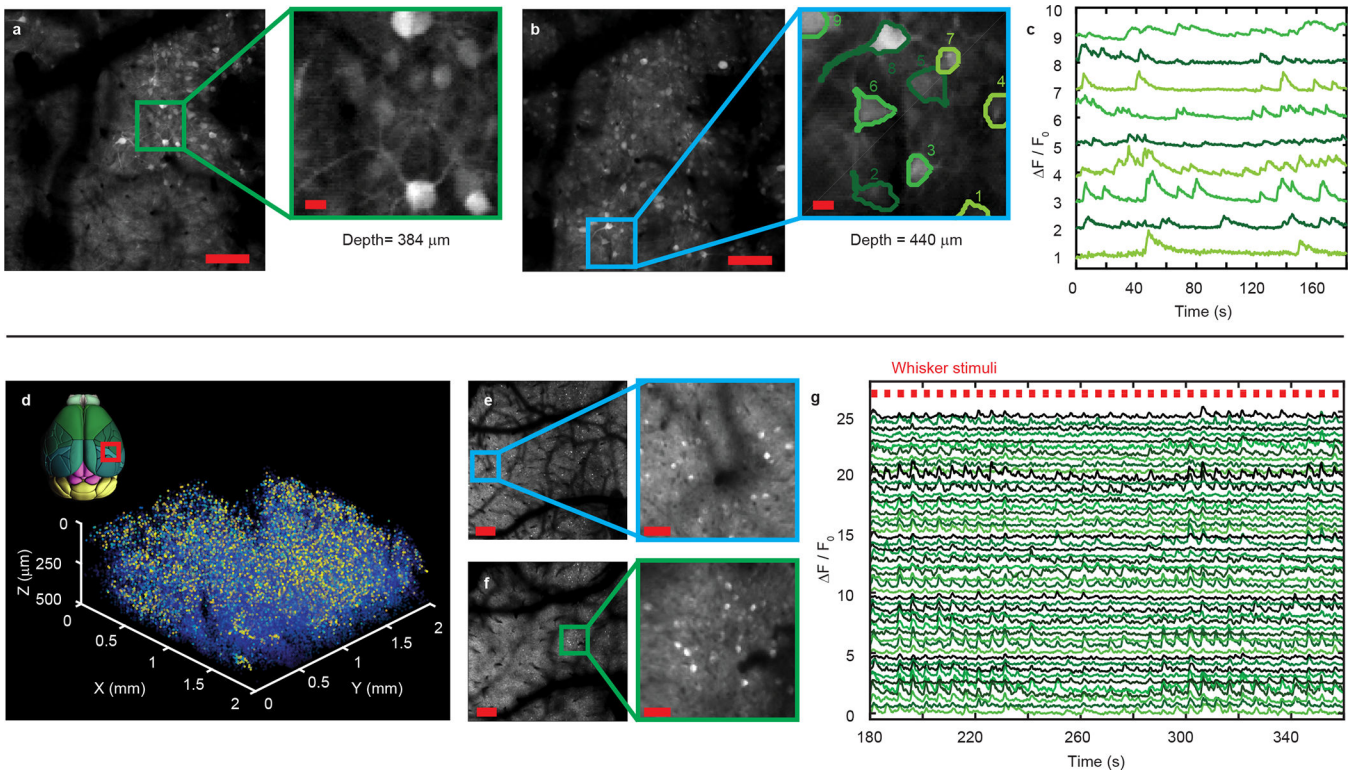

Fig. 4 |. Multi-scale functional imaging with light beads microscopy during whisker stimulation. **a**–**c**, High-resolution volumetric (~600 × 600 × 500 μm^3) imaging of neuroactivity at 9.6 Hz in jGCamp7f-expressing mice. Representative mean projection images of neurons at planes 440 μm (**a**) and 384 μm (**b**) deep, taken from the above volume during a 3-minute recording. Scale bars, 50 μm. Zoomed-in boxed regions are inset, Scale bars, 10 μm. **c**, Representative time series of the nine neurons outlined in the zoomed-in region of the plane in **b**. Offset, 1.0 × Δ*F*/*F*$_0$. **d**–**g**, Recording of 70,275 neurons within a volume of ~2 × 2 × 0.5 mm at 6.7 Hz and 2.8 μm lateral voxel sampling. **d**, 3D rendering of extracted neuron spatial coordinates and maximum projected activity for a 9-minute recording. Transverse brain image reproduced from the Allen Brain Atlas, Brain explorer 2 (ref. [51]). **e**,**f**, mean projection images at 144 and 482 μm depths, respectively. Scale bars, 250 μm. Zoomed-in regions inset scale bars, 50 μm. **g**, Representative time series of 50 whisker-tuned neurons. Occurrences of the stimulus denoted by red marks. Offset, 0.5 × Δ*F*/*F*$_0$.

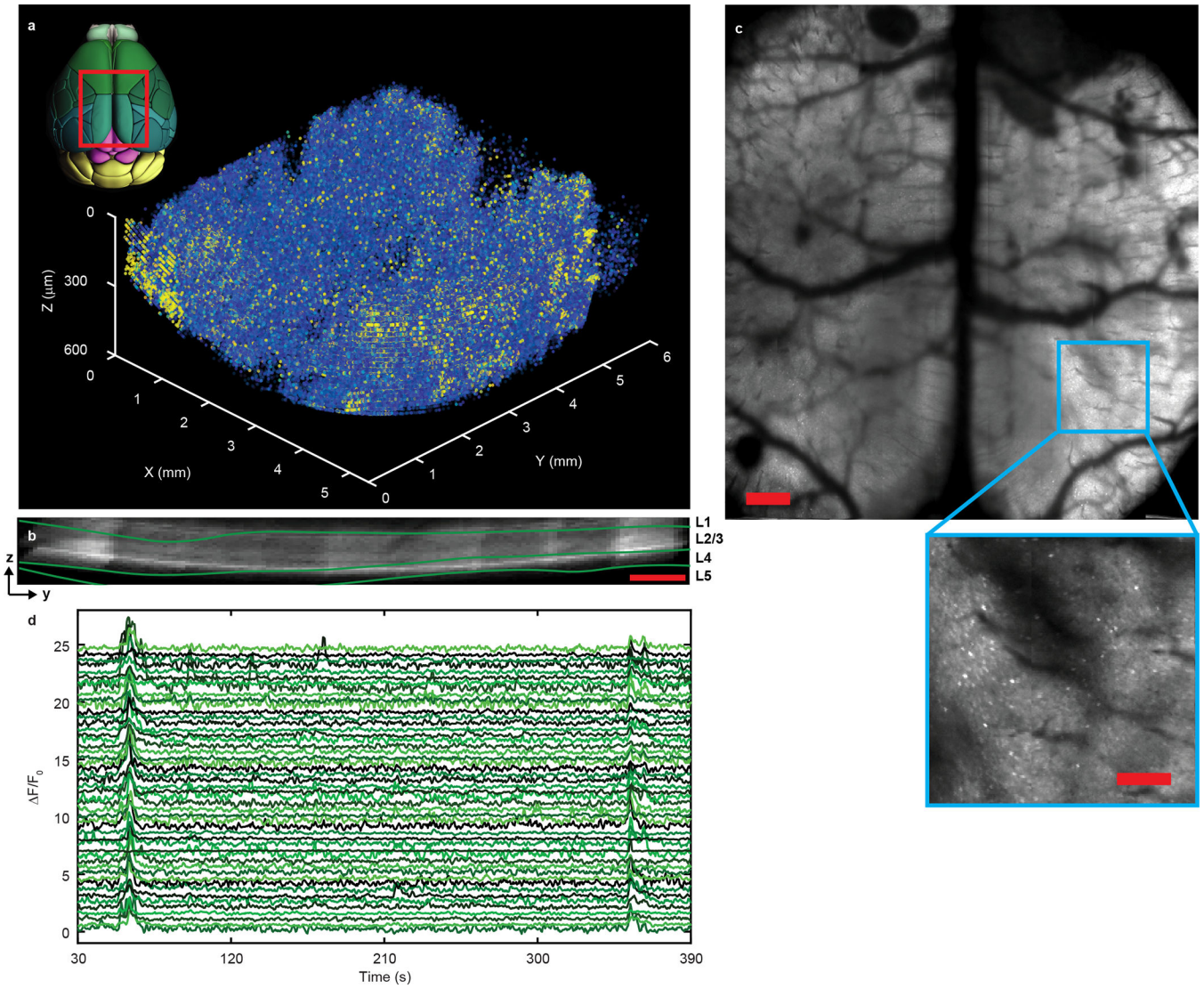

Fig. 5 |. Volumetric recording of 1,065,289 neurons within a volume of ~5.4 × 6 × 0.5 mm at 2.2 Hz in a GCaMP6s-expressing mouse with no external stimulation.

a, 3D rendering of extracted neuron spatial coordinates and maximum projected activity for a 9-minute recording. Transverse brain image reproduced from the Allen Brain Atlas, Brain Explorer 2 (ref. [51]). **b,** *Y*–*Z* projection of the neuron density. Approximate boundaries between cortical layers are denoted with green lines. All depth values are displayed relative to the pia. **c,** Mean projection image from the recording in a at 600 μm depth. Scale bar, 500 μm. Inset, zoomed-in boxed region of **c.** Inset scale bar, 200 μm. **d,** Subset of 50 traces from **e.** Offset, 0.5 × $\Delta F/F_0$.